Icarus 256 (2015) 120–137

Contents lists available at ScienceDirect

Icarus

journal homepage: www.elsevier.com/locate/icarus

Clouds and aerosols on Uranus: Radiative transfer modeling of spatially-resolved near-infrared Keck spectra

Katherine de Kleer [a,*], Statia Luszcz-Cook [b], Imke de Pater [a,c,d], Máté Ádámkovics [a], H.B. Hammel [e,f]

[a] Astronomy Department, University of California, Berkeley, CA 94720, United States
[b] American Museum of Natural History, New York, NY 10024, United States
[c] Delft Institute of Earth Observation and Space Systems, Delft University of Technology, NL-2629 HS Delft, The Netherlands
[d] SRON Netherlands Institute for Space Research, 3584 CA Utrecht, The Netherlands
[e] AURA, 1212 New York Ave. NW, Suite 450, Washington, DC 20005, United States
[f] Space Science Institude, Boulder, CO 80303, United States

ARTICLE INFO

Article history:
Received 1 December 2014
Revised 3 April 2015
Accepted 13 April 2015
Available online 20 April 2015

Keywords:
Uranus, atmosphere
Infrared observations
Adaptive optics
Radiative transfer

ABSTRACT

We observed Uranus in the near-infrared H and K′ bands (1.47–2.38 μm) in 2010 and 2011 with the OSIRIS imaging spectrograph on the Keck II telescope with adaptive optics. In 2010, three years past the equinox, we had a good view of the north polar region while still having access to southern latitudes down to 70°S. In 2011 our observations focused on a moderately bright discrete cloud feature in the middle of the bright circumpolar band at 45°N.

The spatial and spectral resolution of our data allow us to retrieve atmospheric parameters between ~65°S and 75°N via radiative transfer modeling. We test vertical aerosol profiles with combinations of diffuse and compact scattering layers, and find that we can reproduce our equatorial data for a range of cases, provided the deepest detectable aerosol layer is compact and located between 2 and 3 bars, with the higher cloud altitudes corresponding to models with higher methane deep volume mixing ratios. Using a parameterized atmosphere with a diffuse upper haze and a moderately compact lower cloud, we find that both the haze and the cloud reach their maximal optical depth just north of the equator and thin toward the poles. When we fix the abundance of methane with latitude, we find that the bottom cloud shifts to shallower depths at higher latitudes in both hemispheres; for a methane profile with a deep volume mixing ratio of 2.22%, the cloud rises from the 3-bar level equatorward of ±20° to above 2 bars by ±60°. However, when we allow the tropospheric methane abundance to vary according to a parameterized vertical profile, we find that the lower cloud depth is stable in latitude while the methane becomes increasingly depleted toward both poles. In both cases, we find denser aerosol layers and higher methane abundances in the northern hemisphere than the southern, consistent with a seasonal post-equinox trend. In particular, the bright band near 45°N is relatively undepleted in methane, and represents a local peak in the opacity and altitude of the lower cloud. The cloud feature we detected in 2011 falls in the middle of this band. This feature extends from a depth of ~1.3 bars up to the 0.5-bar level. Both CH_4 and H_2S are expected to condense below this level; if the cloud has formed as the result of a convective upwelling event, these are the most likely condensation species.

1. Introduction

Uranus is unique among the giant planets in that its rotational and orbital axes are nearly perpendicular, causing the distribution of solar insolation to differ significantly from the other planets. In addition, Uranus is the only giant planet that appears to have no internal heat source to drive convection and consequently displays far fewer discrete cloud features than the other gas planets in our Solar System. The effect of these differences on global circulation patterns is not well understood; improved models would help generalize our understanding of planetary atmospheric dynamics, which is becoming increasingly relevant to extrasolar planets via the modeling of near-infrared spectra.

The first flyby of Uranus by Voyager 2 in 1986 revealed a quiescent, nearly cloud-free atmosphere during the planet's southern

* Corresponding author at: Department of Astronomy, 501 Campbell Hall #3411, Berkeley, CA 94720, United States.
E-mail address: kdekleer@berkeley.edu (K. de Kleer).

http://dx.doi.org/10.1016/j.icarus.2015.04.021
0019-1035/

summer. In the years surrounding the northern spring equinox in 2007, a multitude of discrete clouds at mid-latitudes were observed, indicating an increase in convective activity. In the years following the equinox, the activity level decreased (e.g. Irwin et al., 2011, 2012a; Sromovsky et al., 2009, 2012c), suggestive of seasonal trends. However, an unexpected surge of cloud activity was detected in August 2014 (de Pater et al., 2015), emphasizing our general lack of knowledge about the seasonal weather patterns and storms on Uranus.

Voyager 2 radio occultation observations were suggestive of a methane condensation cloud near 1.2 bar (Lindal et al., 1987), and West et al. (1991) combined ground-based measurements with Voyager data to identify an optically thin haze layer in the uranian stratosphere, an optically thick methane haze at the 1.2-bar level, and an optically-thin condensation cloud near 3 bars. Since these first results, the existence of a compact methane cloud at the methane condensation level has been debated. Modeling of optical and near-infrared datasets has repeatedly failed to provide any evidence for this cloud (e.g. Sromovsky and Fry, 2007; Karkoschka and Tomasko, 2009; Irwin et al., 2012a,b). Sromovsky et al. (2011), however, do find evidence for it, and attribute the previous failure of detection to the difficulty of resolving it from the higher-opacity cloud layer at 1.4–1.7 bars. In addition, models with too low of a methane mixing ratio would require a longer column of methane to match the observed absorption and would thus position the cloud layer at deeper pressures inconsistent with methane condensation.

Recent disk-resolved observations have permitted an investigation of latitudinal trends in Uranus' atmospheric structure. It has been repeatedly found that the lower cloud deck shifts to higher altitudes toward the poles, and/or the methane abundance decreases (Irwin et al., 2007; Sromovsky and Fry, 2007; Karkoschka and Tomasko, 2009), though these effects are difficult to distinguish from one another. In addition, Uranus sustains bright bands near 45°S and 45°N which have exhibited slow time variability over the past decade. The pre-equinox brightness in the southern band is thought to be the result of a lower methane mixing ratio which results in lower absorption, and may have been accompanied by a lowering in the altitude of the tropospheric cloud (Sromovsky and Fry, 2008). Irwin et al. (2009, 2011, 2012a) and Sromovsky et al. (2009) observed Uranus frequently in the near-IR during and after Uranus' northern spring equinox in 2007 and investigated changes in the distribution of aerosols over this time. Both groups found that the northern bright zone at 45°N has brightened significantly, while the southern zone at 45°S has steadily faded, suggesting that the appearance of these bands may be the result of solar forcing.

In this paper we present new near-infrared spectroscopic observations in the H band (1.47–1.80 μm) from the Keck II telescope in 2010 and 2011. In 2010 we obtained spectra of Uranus at nearly all latitudes, which we use to compare atmospheric models and identify latitudinal trends in the atmospheric structure. From our 2011 observations, we present a high spectral-resolution near-infrared spectrum of an individual cloud feature on Uranus, which we use to model the vertical position and extent of the cloud.

We begin by describing our observations and data reduction and processing methods (Section 2), followed by a description of our radiative transfer code and parameter retrieval techniques (Section 3). We then give an overview of previous atmospheric models of Uranus and describe the models tested in this paper (Section 4). Our analysis and results are organized by three topics: model comparison, latitudinal trends, and discrete cloud feature. Section 5 describes our analysis methodology followed by a discussion of our results for each of these three topics. Our main conclusions are summarized in Section 6.

2. Observations and data processing

2.1. Observations: Keck II OSIRIS

We observed Uranus on UT 2010 July 28 and 2011 July 28 with the 10-meter W.M. Keck II telescope on Mauna Kea, Hawaii. In 2010 we observed a meridional stripe; as Uranus was nearly edge-on to Earth at this date, we were able to observe latitudes from 80°S up to the north pole. Prominent cloud activity on Uranus had been nearly absent in prior years, but in 2011 we observed a cloud feature at mid-northern latitudes.

Spectra were obtained using the OSIRIS imaging spectrometer with adaptive optics (Larkin et al., 2006), using the planet itself for wavefront sensing. The spectrograph uses a 2048 × 2048 pixel Rockwell Hawaii-2 detector, from which data cubes were constructed with spatial dimensions of 16 × 64 pixels, and spectral dimensions of 1651 and 1665 pixels for the H and K′ broadband filters respectively. Observations in both years were made in these two filters, which correspond to wavelengths of 1.473–1.803 μm and 1.965–2.381 μm respectively, with a resolving power of $R \sim 3800$. The 2010 observations used a 0.05″ platescale (field of view = 0.8″ × 3.2″), while the 2011 observations used a 0.02″ platescale (field of view = 0.3″ × 1.3″) to achieve higher spatial resolution on the cloud feature; these platescales correspond to 710 and 284 km per pixel at disk center in 2010 and 2011 respectively. Images were also obtained on these nights with the NIRC2 instrument in H and K′ filters. These images are not used here in our analysis, but are shown in Fig. 1 for context. Table 1 contains details on the observations.

Data were reduced using the standard OSIRIS pipeline, which includes flat-fielding, sky-subtraction, cosmic-ray rejection, wavelength calibration, and data cube assembly. Reduced data cubes were further cleaned to remove bad pixels not identified by the reduction pipeline. The threshold for a bad pixel was five standard deviations from the mean, where the mean and standard deviation were calculated for each wavelength individually. The value of a bad pixel was replaced by the median value of the four neighboring pixels. The percentage of pixels replaced varied with data cube between 0.027% and 0.066%. We also removed the rows of pixels at the edges of the field of view that exhibited anomalous brightness due to lenslet masking errors in the spatially-extended source. Prior to analysis, the data were binned to a spectral resolution of $R \sim 1200$ to match the resolution of our methane absorption coefficients, described in Section 4.2.2.

2.2. Flux calibration and photometry

We observed the standard A-type stars HD 220825 and HD 117774 in 2010 and 2011 respectively for flux calibration and to correct for wavelength dependencies in the atmospheric transmission. The stellar spectra were extracted via the OSIRIS pipeline and aperture photometry, using the largest aperture that fit in the detector area; this corresponded to a radius of 0.45″ in 2010 and 0.18″ in 2011. We assumed that the 0.45″ aperture captured all the light from the star, and estimated the stellar flux lost off the edges of the detector in 2011 by extracting the 2010 stellar spectrum with both 0.18″ and 0.45″ aperture radii and assessing the difference in measured flux density. We determined that the fraction of flux lost off the edges was ~30% and varied linearly in wavelength due to wavelength dependencies in the point spread function (PSF), and we corrected the 2011 stellar spectrum accordingly.

Model spectra for each star were created using the Kurucz model[1] via the method described by Laver et al. (2009), which utilizes the 2MASS[2] H and K magnitudes of the reference stars. For each

[1] http://kurucz.harvard.edu/stars.html.
[2] http://www.ipac.caltech.edu/2mass/.

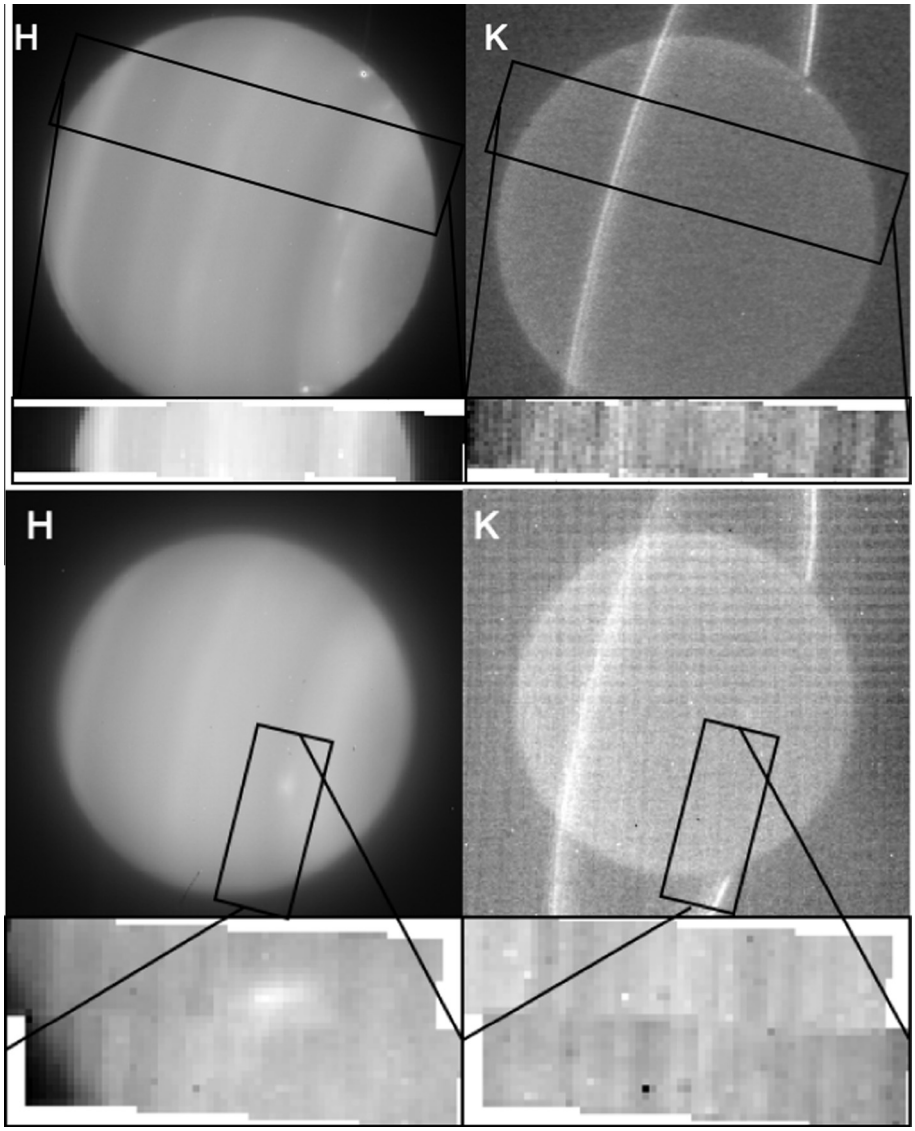

Fig. 1. Observations of Uranus on 2010 July 28 (top) and 2011 July 28 (bottom) in H and K bands. Full-disk images were taken with the NIRC2 imager and demonstrate the rough location of the spectral data with respect to the planet. Insets were obtained with the OSIRIS imaging spectrograph, and are collapsed over the wavelength axis. Because the imaging and spectral data were obtained 1–2 h apart, the location of specific cloud features is not identical between the observations.

Table 1
Keck OSIRIS observations on UT 2010 July 28 and 2011 July 28.

	Time	T_{int}	Filter[a]	Platescale	Airmass
2010 July 28					
Uranus	13:58	300 s	H	0.05″	1.07
	14:04	300 s	H	0.05″	1.07
	14:16	300 s	K′	0.05″	1.07
	14:22	300 s	K′	0.05″	1.07
HD220825	14:46	2 × 5 s	K′	0.05″	1.12
	14:48	2 × 5 s	H	0.05″	1.13
2011 July 28					
HD111133	12:13	10 × 2 s	H	0.02″	1.15
	12:23	10 × 2 s	H	0.02″	1.13
	12:31	10 × 2 s	K′	0.02″	1.12
	12:39	10 × 2 s	K′	0.02″	1.10
Uranus	13:17	360 s	H	0.02″	1.09
	13:24	360 s	H	0.02″	1.08
	13:47	360 s	K′	0.02″	1.06
	13:54	360 s	K′	0.02″	1.06

[a] H, and K′ filters correspond to wavelength ranges of 1.473–1.803 μm and 1.965–2.381 μm respectively.

night, a telluric correction spectrum was constructed by dividing the observed stellar spectrum by the model spectrum for that star. Our spectra of Uranus were then divided by the relevant correction spectrum to minimize the effects of telluric absorption and to flux-calibrate the observations. We did not account for the difference in airmass between the calibration star and planet (<0.06 on both nights); the error contribution from this difference is much smaller than the errors from other sources, such as the uncertainty in the photometry (∼10%).

The weather conditions during our 2011 observations were poorer than in 2010, and the data quality was less consistent over the time of observation. We therefore correct the 2011 data for atmospheric transmission via the 2011 stellar observations, but calibrate the absolute flux from our 2010 data via a wavelength-independent multiplicative factor of 1.3. This factor is calculated so that a feature-free region of Uranus' disk with matching latitude and emission angle gives the same H-band reflectivity between the two years, and its magnitude is consistent with the level of error introduced by non-photometric observing conditions. The shape of the spectrum in this region matches closely between

dates after this scaling is applied, lending support to our choice of wavelength independence in the correction factor.

2.3. Navigation

We calculate the latitude, longitude, and incident and emission angles of our datasets at quarter-pixel resolution by a limb-fitting method based on that of Lii et al. (2010): a model grid of the planet with longitude and latitude lines[3] is fit by eye to a wavelength-collapsed H-band image of the planet using the limb for reference. This procedure is repeated five times, and the average of the fits is taken as the final navigation. The accuracy of this method is limited by the accuracy with which the curvature of a small piece of limb can be matched to the model by eye. In the 2010 data, which covers a larger portion of the limb, we estimate the H-band navigation is accurate to ± 1 pixel, corresponding to 710 km or 1.6 degrees of latitude at the equator; in the 2011 data the fit is accurate to ± 2 pixels, corresponding to 570 km or 1.3 degrees of latitude.

Uranus is nearly invisible in our K′-band OSIRIS observations (see Fig. 1), and we are unable to distinguish the location of the limb on either date. Though we do not include these observations in our analysis, the absence of light from the planet at these wavelengths, which probe Uranus' atmosphere above 1.0 bar, provides a check on our models.

2.4. Data uncertainties

An accurate understanding of the uncertainties in our data is essential for getting the most accurate model fits. The size of the uncertainties entering the fits affects the uncertainties on the derived parameters as well as the degree to which one model is preferred over another, while the spectral variation in the uncertainties enters the fits as weights across the spectral axis and can therefore have a significant effect on the derived parameters themselves. In this section we briefly discuss the various types of uncertainty in our data and how we quantify and address them: Section 2.4.1 addresses the rms of the data and the effects of band shape, while Section 2.4.2 describes uncertainties in the photometric offset and slope.

2.4.1. Noise

The OSIRIS instruments records >1000 spectra on a single detector simultaneously by packing spectra very close together. Rectifying the resultant 2-d image into a 3-d data cube thus requires extracting each spectrum using the precise PSF of each individual lenslet at every wavelength (Larkin et al., 2006). There are numerous potential noise contributions, due to e.g. the filter shape, the effects of detector location, the contamination of faint spectra by neighboring bright spectra on the detector, and an imperfect spectral extraction due to instability in each individual PSF. We estimate the noise in the data empirically, and consider two types of noise contributions: pixel-to-pixel scatter within a spectrum, or spectral noise, and pixel-to-pixel scatter when considering a wavelength cut, or spatial noise.

We find a spectral noise of $\sim$2% over most of the H band, rising to nearly 6% at the band edges, derived from the spectra of both Uranus and the standard star. We assess spatial noise at each wavelength by comparing neighboring pixels on a featureless region of Uranus' disk; however, we note that we do not expect any region of Uranus' disk to be perfectly uniform, due to physical differences across Uranus' atmosphere as well as the different viewing geometry at each pixel. We find that the spatial noise at a given wavelength is not a fixed fraction of the total brightness at that wavelength, and can be approximated by a step function with a value of 0.0005, in units of fractional reflected sunlight, at wavelengths >1.62 μm where Uranus is very faint, and 0.001 at shorter wavelengths where Uranus is brighter. This constitutes >2% of the signal at all wavelengths, and is added in quadrature to the spectral noise term to produce our final uncertainty spectrum. Because the uncertainty spectrum has a signal-dependent term, it is calculated separately for each spatial location and varies slightly across Uranus' disk.

2.4.2. Photometry

We estimate the uncertainty in the photometry of our data and stellar calibration based on a comparison between successive integrations on the same target. In 2011 we obtained two consecutive integrations on the reference star. Their difference is 5–10% in median flux density, with a linear trend in wavelength of $\sim$6% over the 1.45–1.8 μm window. This level of consistency between stellar integrations is similar to what we have seen in past observations with the same instrument (e.g. de Kleer et al., 2013). We did not have multiple observations of the reference star in 2010, but note that weather conditions and data quality were both much better in 2010 than 2011.

Our observations of the planet itself give a more informative estimate of the quality of the photometry. On each date our observations of Uranus consist of two mosaicked integrations with a small overlapping region of 450 pixels in 2010 and 120 pixels in 2011. We extract the median spectrum from this region of overlap in each observation, and estimate the difference between the successive observations. We find that the difference is best modeled as a small offset whose magnitude is <5% of the signal from the planet in the 1.5–1.6 μm region. We add a wavelength-independent factor to each observation so that the overlapping regions on each date match the median of the two successive observations, and incorporate the value of this offset into our uncertainties.

The long-wavelength (>1.62 μm) region of the spectrum differs in slope between successive observations; this effect is most pronounced in the 2011 observations, and is mostly likely due to wavelength-dependent differences in atmospheric extinction and the PSF. Our atmospheric models predict a flat slope over this region, with variations due to methane absorption occurring only on smaller wavelength intervals; we therefore flatten this slope in our data before fitting the models.

3. Radiative transfer calculation and parameter retrieval

3.1. Radiative transfer calculation

We model the atmosphere of Uranus from the high stratosphere (0.1 mbar) down to 8 bars in the troposphere with a gaseous background atmosphere composed of molecular hydrogen, helium, and methane with additional layers of scattering particles. The models are parameterized by the vertical profiles of temperature and methane abundance, and by the locations and properties of the scattering layers; these parameters are discussed in detail in Section 4. We calculate near-infrared spectra for each model via our radiative transfer code, which is adapted from a code initially developed for Titan (Ádámkovics et al., 2007) and previously adapted for Neptune (Luszcz-Cook et al., 2010). We use the H_2–H_2, H_2–He and H_2–CH_4 collision-induced absorption coefficients from Borysow et al. (1985, 1988) and Borysow (1991, 1992, 1993) assuming an equilibrium ortho/para hydrogen ratio. Our model uses the correlated-k approximation for methane absorption, and we use the k-coefficients of Sromovsky et al. (2012a) based on their new M5 line list compilation, which are tabulated at intervals of 5 cm^{-1}.

[3] Ephemeris obtained from JPL's HORIZONS system: ssd.jpl.nasa.gov/horizons.cgi.

The radiative transfer equations are solved using the two-stream approximation (Toon et al., 1989). This method treats only the hemisphere-averaged scattering in the forward and backward directions, sacrificing some degree of accuracy for computational efficiency. To assess the errors introduced by the use of this approximation, we compare model spectra calculated using the two-stream method with those produced using the *disort* (Discrete Ordinates Radiative Transfer) program (Stamnes et al., 1988), assuming a single Henyey–Greenstein phase function. This phase function can be expanded as an infinite series of Legendre polynomials, and the number of terms used in the calculation determines how completely the phase function is described. The number of streams must match the number of terms for the scattering information to be accurately represented in the calculation. We increase the number of terms and ordinates used in the calculation until the addition of more terms does not affect the model spectrum, indicating that we have specified the phase function as accurately as the data can distinguish. We find that the model spectra calculated in this way deviate from those calculated using the two-stream approximation by between <5% and ~10% depending on the wavelength, emission angle, and atmospheric structure. We use these differences to place uncertainties on our models as follows. We first calculate a *disort* spectrum for the best-fit model found using the two-stream approximation for each atmospheric structure and latitude. We then re-run the two-stream fits with the differences between the *disort* and *two-stream* model spectra as an additional uncertainty term. This term has the effect of weighting different spectral regions based on how robust the model is in that region to the number of streams; incorporating these weights results in minor differences in the retrieved parameters. The final uncertainties on our retrieved parameter values thus reflect both the uncertainties in our data and the systematic error introduced by the use of the two-stream approximation in our calculations.

3.2. Parameter retrieval

Our parameter retrievals utilize Markov chain Monte Carlo (MCMC) methods for parameter estimation and uncertainties. The goal of MCMC methods is to approximate a physical probability distribution by constructing a Markov chain whose equilibrium distribution is the desired distribution (e.g. MacKay, 2003). For a given k-dimensional vector of parameters θ and data $y = (y_1, \ldots, y_n)$, we would like to know $p(\theta|y)$, the posterior probability distribution of each parameter given the data, where

$$p(\theta|y) = \frac{1}{f(y)} p(\theta) p(y|\theta) \tag{1}$$

and $f(y)$ is a normalization constant that depends only on the data. Determining the posterior distribution requires a prior distribution $p(\theta)$ incorporating any prior knowledge that informs the probability distribution, and a likelihood function $p(y|\theta)$. The MCMC algorithm generates a random walk in parameter space that draws a representative set of samples from the posterior distribution. Once these samples have been generated, the probability distribution for each free parameter can be read off the distribution of values drawn for that parameter, after an initial burn-in phase.

We use an affine invariant ensemble MCMC method in which an ensemble of chains is simultaneously constructed, with the subsequent step in each chain dependent on the current position of each individual chain within k-dimensional parameter space (Goodman and Weare, 2010). We employ the Python **emcee** implementation of this algorithm by Foreman-Mackey et al. (2013), which has been used successfully in various astrophysical applications.

We provide a guess for each parameter, and initialize each chain at a different set of parameters drawn randomly from a Gaussian distribution centered at the guess values. Our prior distributions are log-flat and span many orders of magnitude, consistent with a high degree of initial uncertainty in the true parameter values. The Markov Chain random steps seek to maximize the likelihood function, or the likelihood of drawing our data y given our model and a set of parameters θ. In the case of χ^2 fitting, the likelihood function is given by

$$L = \prod_{i=1}^{n} \left(\frac{1}{2\pi\sigma_i^2} \right)^{1/2} \exp\left(-\sum_{i=1}^{n} \frac{(y_i - f(x_i))^2}{2\sigma_i^2} \right) \tag{2}$$

and

$$ln(L) = C - \chi^2/2, \tag{3}$$

where C is a constant that depends on the data but is independent of the model.

For each fit, we create 150 simultaneous chains. The algorithm typically converges within a few hundred steps, and we run each ensemble for a minimum of ~100 steps after convergence to ensure the robustness of the solution. A demonstration of this technique, including chains, their corresponding parameter distributions, and parameter correlations, is shown in Figs. 2 and 3.

3.3. The Deviance Information Criterion

While the MCMC algorithm yields accurate parameter estimation and uncertainties for a given model, it does not give a direct metric for comparison between different models. Using a comparison of χ^2 between models can be misleading because it does not take into account model complexity, which is not simply a function of the number of inputs. For the purpose of model comparison, we employ the Deviance Information Criterion (DIC) proposed by Spiegelhalter et al. (2002). The DIC includes a standard term for goodness-of-fit with a penalty term for model complexity, and considers the full posterior distribution of each parameter, allowing comparison of the models themselves instead of their single best-fit manifestations. This metric is particularly convenient because it is simple to calculate from the output of MCMC simulations.

The DIC employs the deviance to measure both goodness of fit and model complexity, where the deviance $D(\theta)$ is defined as the difference in the log-likelihoods between the fitted model and a perfect fit to the data.

$$D(\theta) = -2lnL(y|\theta) + 2lnf(y), \tag{4}$$

where $L(y|\theta)$ is the likelihood function for the data y given the parameter set θ and $f(y)$ is a function of the data alone, and therefore cancels when considering the difference in deviance between models for the same dataset (Dempster, 1974).

The goodness of fit is given by the posterior expectation of the deviance $\overline{D(\theta)}$, so that smaller values correspond to better fits. The models are penalized for complexity based on the effective number of parameters p_D, defined as the difference between the posterior mean of the deviance $\overline{D(\theta)}$ and the deviance evaluated at the posterior mean of the parameters $D(\bar{\theta})$:

$$p_D = \overline{D(\theta)} - D(\bar{\theta}). \tag{5}$$

The DIC is then defined as the sum of these two components:

$$\mathrm{DIC} = \overline{D(\theta)} + p_D = D(\bar{\theta}) + 2p_D. \tag{6}$$

These parameters are calculated from the output from our MCMC simulations: $\overline{D(\theta)}$ is the mean of the distribution of likelihood values calculated at values sampled from the k-dimensional probability

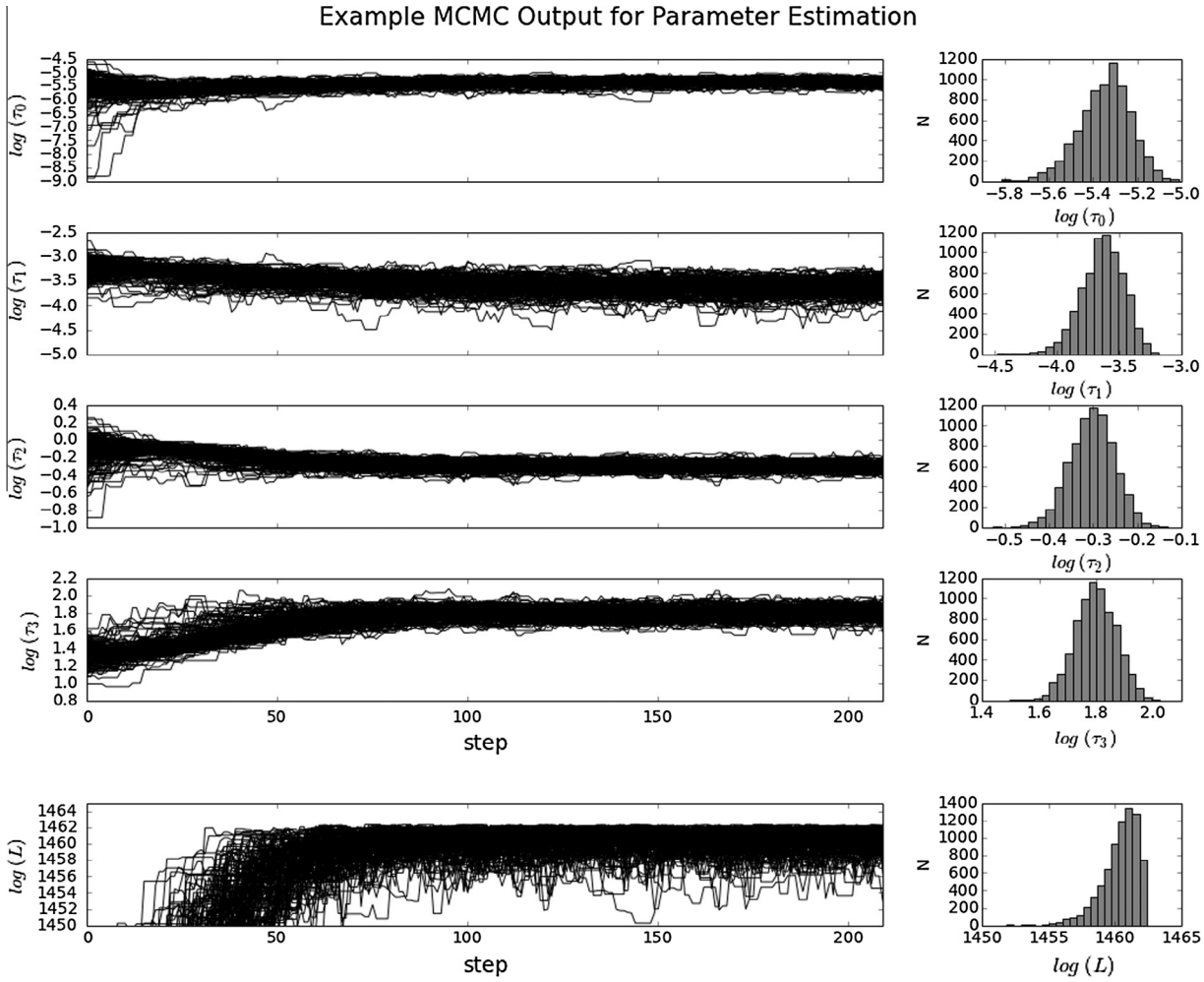

Fig. 2. Demonstration of the use of Markov Chain Monte Carlo (MCMC) simulation for parameter estimation. Plots on the left show the values taken on by each of 150 walkers at each step for an example simulation using the Diffuse Haze (DH) model, which has four layers with fixed boundaries at {0.1, 1.2, 2.0} bars and the optical depth of each layer as free parameters: $\{\tau_0, \tau_1, \tau_2, \tau_3\}$. The values for the likelihood L at every step is shown in the bottom panel. The chains have converged by step 150 in this example; the histograms of the post-convergence chains are plotted to the right. These represent the retrieved probability distribution for each parameter.

distribution of parameter values, and $D(\bar{\theta})$ is the deviance calculated at the expectation of the simulated values of θ.

4. Atmospheric models

In this section we discuss in detail the various parameters that enter our atmospheric models, including the choices previous authors have made and the reasoning behind our adopted models. Sections 4.1 and 4.2 address the particle scattering properties and the treatment of methane. In Section 4.3 we review atmospheric structure models that have been used by previous authors to fit observations, and describe the three models we choose to explore in Section 4.4.

4.1. Particle scattering properties

Scatterers in a model atmosphere are described by their size distribution $f(R)$, single-scattering albedo ϖ_0, scattering phase function $p(\theta)$, and complex refractive index n, which in turn determine the cross-sections for scattering, absorption, and extinction. Cold (<100 K) methane ice, which dominates the scattering in ice giant planets, has a wavelength-dependent refractive index which is in the vicinity of $1.4 + 0i$ in the near-infrared (Satorre et al., 2008; Martonchik et al., 1984), and we adopt this value in our models. The single-scattering albedo predicted by Mie theory is 1.0 for conservative scattering; we use the value of $\varpi_0 = 0.75$ empirically determined from limb-darkening observations (Sromovsky and Fry, 2007). While this estimate may be biased by the use of older methane absorption coefficients less appropriate for Uranus' atmospheric conditions, Irwin et al. (2011, 2012b) derived comparable values based on Uranus' H-band spectra, using the updated methane coefficients of Karkoschka and Tomasko (2010) and the recent line data from Campargue et al. (2012).

The simplest distribution of particle sizes is a delta function at a specific particle radius. However, the modified gamma distribution describes the size spectra of condensing aerosols particularly well (Williams, 1985), and is often used in this context. For a particle size population with mean and variance μ and σ, this distribution has the form

$$f(r; k, \theta) = \frac{r^{k-1} e^{-\frac{r}{\theta}}}{\theta^k \Gamma(k)} \tag{7}$$

where the scale $\theta = \sigma/\mu$, the shape parameter $k = \mu^2/\sigma$, and $\Gamma(k)$ is the gamma function evaluated at k. The form of this distribution is shown for the combinations of input parameters used in this work in Fig. 4. We use this function to model our particle sizes, with average radius values fixed at 0.1 μm for the upper atmosphere, and in the 0.6–1.2 μm range at deeper levels, consistent with physical

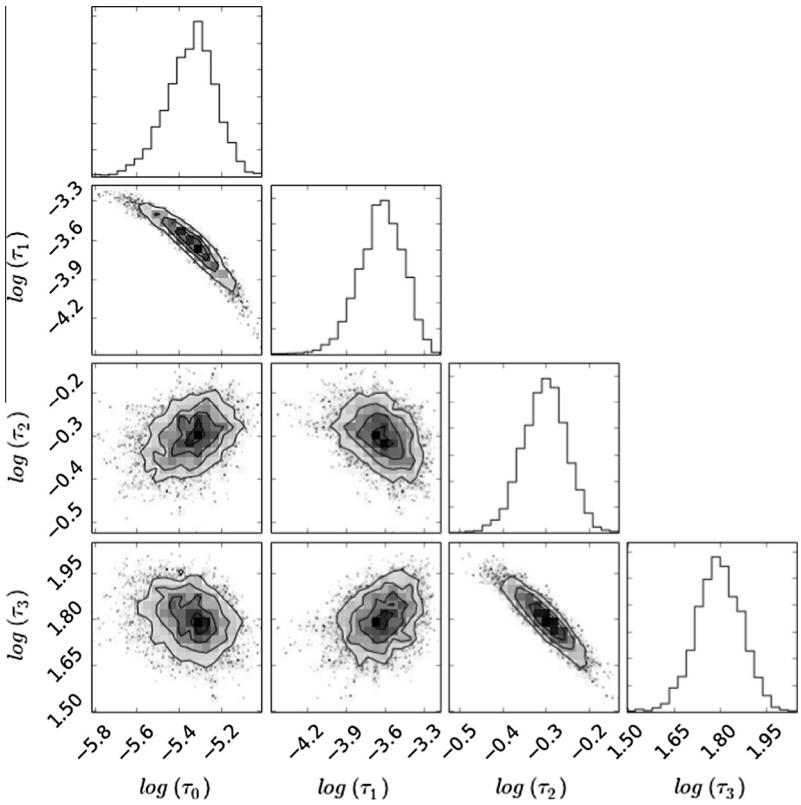

Fig. 3. Demonstration of parameter correlations from MCMC simulation, for the same run shown in Fig. 2. Scatterplots show the values taken on by each pair of parameters at every step, and histograms show the derived probability distribution for each parameter as in the previous figure.

predictions. Pollack et al. (1987) predict, based on photochemical and microphysical modeling, that stratospheric scattering particles are likely to be dominated by ethane, acetylene, and diacetylene gasses produced from UV photolysis of methane above the 0.1 mbar level and descending to their condensation pressures of 14, 2.5 and 0.1 mbar for these three species respectively, and are ∼0.1 μm in size. Deeper in the atmosphere, where hazes are most likely composed of condensed CH_4 or H_2S, particle sizes may be closer to 1.0 μm.

While the scattering particles may have complicated shapes and phase functions, our observations are not sensitive to these details and we find that a simple scattering phase function is sufficient to fit our data. We specify this phase function with a single asymmetry parameter g that sets the fraction of back- and forward-scattering; a value of $g = 1$ corresponds to pure forward scattering, and $g = -1$ to pure backscattering. The wavelength dependence of g is calculated from Mie theory. The parameter g is strongly dependent on the particle size; the calculated asymmetry parameters for the wavelengths and particle size distributions used in this paper are shown in Fig. 4.

4.2. Temperature and methane profiles

Lindal et al. (1987) derived temperature and methane profiles for the outer atmosphere of Uranus consistent with radio occultation observations. These profiles, labeled A–F, are characterized by their deep methane mixing ratio which ranges from <2% for profile A to 4% for profile F. Sromovsky et al. (2011, 2014) created additional methane profiles (D1, DE, E1, EF, F1, FG, and G) with associated temperature profiles, consistent with the same observations. The wavelength range we are analyzing is less suited to constraining the deep methane mixing ratio than previous observations; we therefore limit our models to three methane profiles (D1, E1, and F1 with deep volume mixing ratios of 2.22%, 3.20% and 4%) with associated temperature profiles.

For each new methane profile, Sromovsky et al. (2011) calculated corresponding values for the helium mixing ratio that both match the occultation observations and achieve methane saturation in the putative condensation region. We use these values in our models; at 0.126, 0.122, and 0.1155 for the D1, E1, and F1 profiles respectively, they are all within $\sim 1\sigma$ of the value of 0.15 ± 0.033 determined earlier by Conrath et al. (1987).

4.2.1. Methane depletion

Recently, numerous authors have found that invoking a greater methane abundance over the equator than the poles is required to fit observations (Karkoschka and Tomasko, 2009; Sromovsky et al., 2011, 2014; Irwin et al., 2012a; Tice et al., 2013). Sromovsky et al. (2011) found they were unable to fit both equatorial and polar spectra with the same vertical distribution of methane, and constructed depleted methane profiles with various depletion degrees and shapes to fit the polar data. They argue that depletion must occur only at shallow depths because a latitudinal gradient in mixing ratio at great depths would produce winds inconsistent with what is observed on Uranus. However, this is seemingly at odds with microwave observations that imply depletions and latitudinal differences down to tens of bars (de Pater et al., 1989; Hofstadter and Butler, 2003). Irwin et al. (2011, 2012a) and Tice et al. (2013) also found evidence for an enrichment of methane at the equator over mid-latitudes, and note that the apparent variation in cloud top pressure with latitude may disappear when this methane gradient is considered.

We model methane depletion using the Sromovsky et al. (2011) "proportionally descended gas" profile. While undepleted profiles have an abrupt transition in methane abundance at a pressure of 1.2 bars where the temperature becomes low enough for methane

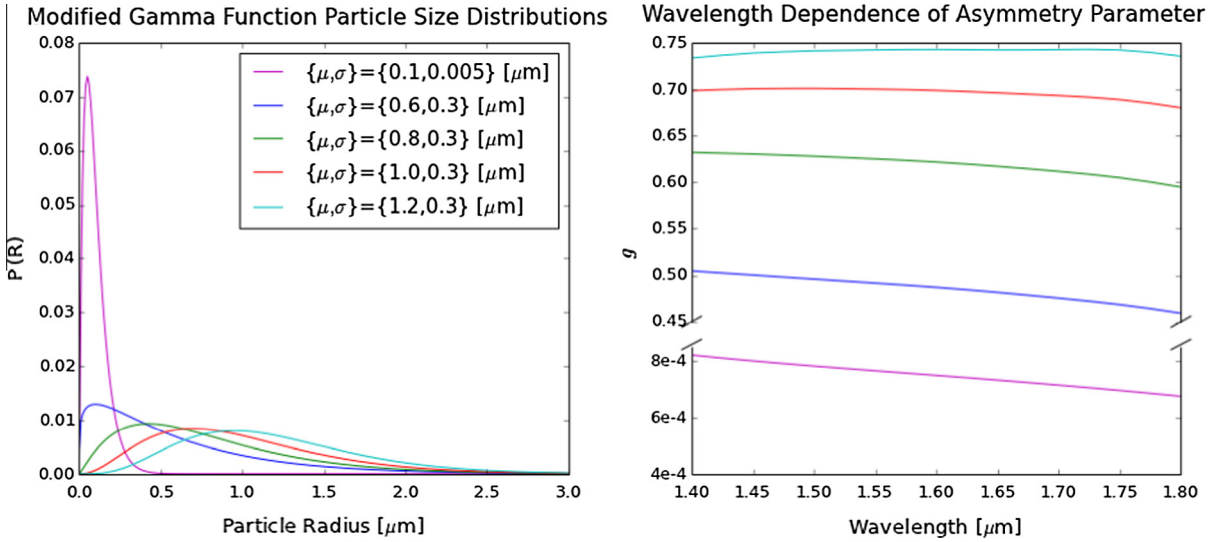

Fig. 4. Particle size distributions and phase functions. [Left] Modified gamma particle size distributions used in our analysis. [Right] The asymmetry parameter g as a function of wavelength, as derived from Mie theory for the particle size distributions of the corresponding colors in the left plot. (For interpretation of the references to color in this figure legend, the reader is referred to the web version of this article.)

to condense out, these depleted profiles increase methane gradually with increasing depth by shifting the mixing ratio profile $\alpha(P)$ down to increased pressure levels $P'(\alpha)$ using the equation

$$P' = P \times [1 + (\alpha/\alpha_d)^{vx}(P_d/P_c - 1)] \text{ for } P_{tr} < P < P_d, \quad (8)$$

where P_d is the pressure depth at which the revised mixing ratio $\alpha = \alpha(P')$ equals the uniform deep mixing ratio α_d, P_c is the pressure at which the methane condensation temperature is reached, P_{tr} is the tropopause pressure, and vx controls the shape of the profile in the depleted region. We fix the value of vx at 2.0, which Sromovsky et al. (2011, 2014) suggest provides a good fit to the data.

Such a profile smoothly depletes the methane in the upper troposphere (above P_d) without changing the methane abundance in the deeper atmosphere, such as may occur in a circulation system in which dry air from $P < P_c$ descends to a depth of P_d. The depletion of methane below the tropopause brings the average methane abundance below saturation in this region; this inhibits global methane condensation, though clouds may still condense locally. The dry air above P_c required to explain the depletion requires a methane-removal mechanism such as a condensation cloud. These two requirements are reconciled in (*a*) a scenario in which condensation is occurring in local convective cells in a region of overall downwelling, or (*b*) a global system in which methane is condensing in equatorial regions, and the dried-out air above the cloud layer is then distributed to high latitudes by a hemispheric circulation cell, depleting the methane in polar downwelling regions. The latter scenario is discussed in detail by Sromovsky et al. (2011).

Fig. 5 demonstrates the construction of a depleted methane profile in panel (*a*), and shows the three methane profiles D1, E1, and F1 with two example depletion depths in panel (*b*). The methane depletion profile is parameterized by a single value: the depletion depth P_d. However, we note that the model allows depletion depths that may be deeper than our observations are sensitive to, in which case the retrieved depths are heavily dependent on the depletion profile and may not be physically meaningful.

4.2.2. Methane coefficients

Over the past decades, significant advances have been made in our knowledge of methane absorption properties and their extrapolation to the path lengths and temperatures of the uranian atmosphere, resulting in an ability to fit observed near-infrared spectra increasingly well. Sromovsky et al. (2012a) and Irwin et al. (2012b) assess the ability of different methane coefficients and absorption line shapes to match measured spectra of Uranus' atmosphere. In the H-band spectral region, both groups independently find that recent improvements in line lists greatly improve their ability to fit measured spectra with Uranus atmospheric models. Irwin et al. (2012b) find the best match for the Hartmann et al. (2002) line shape, while Sromovsky et al. (2012a) prefer a far-wing line shape between that of Hartmann et al. (2002) and de Bergh et al. (2011). We adopt the latter line shape, using the correlated-*k* approximation (Lacis and Oinas, 1991) for improved speed, with the k-coefficients calculated by Sromovsky et al. (2012a). These coefficients are tabulated at a wavenumber interval of 5 cm^{-1}, and our data are binned to match this resolution prior to fitting.

4.3. Atmospheric structure models

Previous authors have used a variety of atmospheric structures and particle scattering properties to fit spectra of Uranus at near-infrared and optical wavelengths. Model atmospheric structures generally fall into two categories: atmospheres with aerosols confined to vertically-localized layers, and atmospheres full of a diffuse haze that varies in opacity with altitude. These structures are reviewed below before a description of our model structures.

4.3.1. Discrete cloud models

While atmospheres with a single aerosol layer have been found inadequate at modeling observations, models with two discrete cloud layers have often been used. These are typically parameterized as an upper haze (UH) based between 1.0 and 0.5 bars and a lower tropospheric cloud (TC) below 1.0 bars. Irwin et al. (2012a) note that they are able to fit the H-band spectrum with many different vertical cloud distributions ranging from continuous to discrete, but that the two-cloud model is sufficient and minimizes free parameters and assumptions.

Using such a model with near-infrared data and assuming a continuous distribution of micron-sized particles with a wavelength-independent Henyey–Greenstein phase function with an

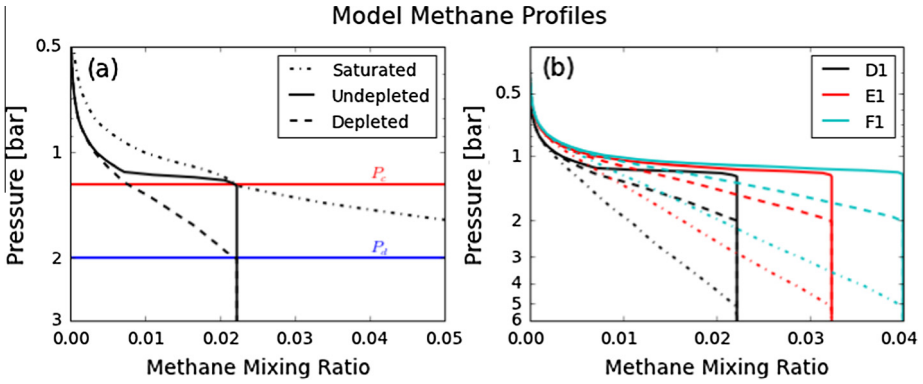

Fig. 5. Model methane profiles: (a) The saturated methane profile and undeleted profile for the D1 case, with a depleted profile assuming a depletion depth of 2.0 bars, the depth at which the depleted profile reaches the undepleted deep methane mixing ratio. Horizontal lines show the pressure P_c at which the methane condensation temperature is reached, and the depletion depth P_d. (b) The D1, E1, and F1 profiles (Sromovsky et al., 2011). Solid profiles are undepleted, dashed profiles are depleted to 2.0 bars, and dash-dotted lines are depleted to 5.0 bars.

asymmetry parameter $g = 0.7$ and refractive index of $1.4 + 0i$, Irwin et al. initially found extended clouds with peak opacities at the 2–3 and 8–10 bar levels at equatorial latitudes (2007), though the use of improved methane k-coefficients decreased the significance of the deeper cloud (2012a). They find that very close fits to 1.4–1.6 μm spectra require particles that become less scattering toward the longer wavelengths, and vary the single-scattering albedo smoothly across these wavelengths to fit the data, an approach also employed by Tice et al. (2013). These authors test a range of fixed particle sizes for each cloud, and find a weak preference for 0.1-μm particles in the UH and a strong preference for 1.35-μm particles in the TC, approximating all particle phase functions as Henyey–Greenstein functions with a wavelength-independent asymmetry parameter of $g = 0.7$. Sromovsky et al. (2006) also used a two-cloud model to successfully fit near-infrared spectra obtained in 1975 by Fink and Larson (1979), but they note that a six-cloud model that permits a more complex distribution of opacity provides a much better fit to the observations.

4.3.2. Diffuse haze models

Karkoschka and Tomasko (2009) test a model of discrete condensation clouds against STIS spectroscopic Hubble data. The best-fit two-cloud model had clouds at 1.4 and 3 bars, consistent with the locations of peak opacity found by Irwin et al. (e.g. 2012a). However, they find a much better fit with an atmospheric model of extended haze layers without compact clouds, and argue that the frequent lack of detection of a condensation cloud at 1.2 bars indicates that the observed opacity may be due to a vertically-extended haze of aerosols, with aerosol production occurring near 1.2 bars followed by subsequent descent to lower altitudes on long timescales. Their model consists of low-opacity layers in the stratosphere and upper troposphere (0.1–1.2 bar) and higher-opacity middle and lower tropospheric layers (1.2–2 bars and >2 bars respectively). They adopt stratospheric scatterers with a wavelength-dependent imaginary index of refraction, scattering efficiency, and single-scattering albedo, and tropospheric scatterers with a wavelength-dependent single-scattering albedo and a double Henyey–Greenstein particle phase function with parameters $g_1 = 0.7$ and $g_2 = -0.3$ and a wavelength-dependent weight f_1 that varies from 0.470 to 0.940 as λ increases from 310 to 940 nm. With these particle properties, they find a stratospheric particle size of ~0.1 μm, with larger (~1-μm) particles at deeper levels.

4.3.3. Combination models

Sromovsky et al. (2011) modified the four-layer diffuse model of Karkoschka and Tomasko (2009) to include compact condensation clouds in addition to the haze layers. They replaced the middle tropospheric haze layer with two compact cloud layers and replaced the lower tropospheric haze layer by a compact cloud at 5 bars, which was needed to fit their spectrum near 0.56 and 0.59 μm, though the pressure level and vertical extent of this cloud were not well constrained. They later adapted this model to fit 1.48–1.64 μm near-IR spectra by neglecting the compact cloud at 1.2 bar because they found that the data could not distinguish individual contributions at this pressure level (Sromovsky et al., 2012a). For tropospheric aerosols, they adopted the particle scattering properties of the Karkoschka and Tomasko (2009) model, but extended the wavelength-dependence of the phase function into the near-infrared assuming 0.8-μm Mie particles.

4.4. Our models

We model our data with three different atmospheric structures based on those described in Section 4.3; our models are summarized here. Our temperature and methane profiles and our adopted particle scattering properties are described in Sections 4.1 and 4.2. We parameterize the vertical distribution of aerosol density within a scattering layer by the fractional scale height H_{frac}, which is the ratio of the scale height of the aerosols to that of the background gas.

4.4.1. Two-cloud model [2C]

Our two-cloud model is based on the models by Irwin et al. (2012a) and Tice et al. (2013). It consists of a tropospheric cloud (TC) and upper haze (UH). The UH is constrained to lie at altitudes above 1.0 bar, and the particles follow a modified gamma distribution of sizes with mean and variance of 0.1 and 0.005 μm, consistent with the mean particle size preferred by Tice et al. (2013). The TC is a layer of larger particles (~1 μm) in the deeper troposphere, below 1.0 bar. Our model differs from that of Irwin et al. (2012a) and Tice et al. (2013) by our choice to vary the particle phase function in wavelength based on Mie theory while keeping a wavelength-independent single-scattering albedo. The free parameters in this model are the base altitude, optical depth at 1.6 μm, and fractional scale height $\{P_{max}, \tau, H_{frac}\}$ of each layer.

4.4.2. Diffuse haze model [DH]

Our diffuse haze model consists of four continuous hazes with the fixed pressure boundaries used by Karkoschka and Tomasko (2009): 100 mb, 1.2 bar, and 2.0 bar. The aerosols are evenly mixed with gas within each layer ($H_{frac} = 1.0$). The uppermost layer consists of small (~0.1 μm) particles, while the lower layers contain

larger (~1.0 μm particles); the exact particle size distributions used in modeling are described in Section 5.1.1. We fit only for the total 1.6-μm optical depth τ of each haze layer, for a total of four free parameters.

4.4.3. Modified diffuse haze model [MDH]

Our third model is motivated by the model used by Sromovsky et al. (2012a) to fit near-infrared spectra of Uranus. This model is identical to our diffuse haze model except that we model the bottom layer (below 2.0 bars) as a compact cloud instead of a diffuse haze, and leave its depth P_{bottom} as a free parameter with the compactness requirement $P_{top} = 0.9P_{bottom}$. This cloud is assumed to have the same scattering properties as the other tropospheric layers.

5. Analysis and discussion

Our analysis is divided into three steps: we first use equatorial data to test various choices for atmospheric structure, methane profile, and particle size. We then fix the atmospheric structure and fit our entire dataset to assess variations in the depths and opacities of the aerosol layers with latitude. Finally, we fix these properties according to the best model fit to the 2010 data at a latitude of 45°N, and use the spectrum of the discrete cloud feature observed in 2011 to fit for its depth and vertical extent. Our methodology and results are presented for the model comparison in Section 5.1, for the latitudinal analysis in Section 5.2, and for the discrete cloud in Section 5.3. A discussion of these results in the context of global circulation models is given in Section 5.4, and our conclusions are summarized in Section 6.

5.1. Compact/diffuse profile comparison

5.1.1. Analysis

We perform tests of the atmospheric structure, particle size distribution, and methane profile using equatorial data (between 10°S and 10°N in latitude): for each of the 2C, DH, and MDH models introduced in Section 4.4, we perform fits for the three cases of methane profile {D1, E1, F1} (see Section 4.2) and four cases of particle size distribution. An overview of the free and fixed parameters of each model is given in Table 2. Each model includes two distinct sets of scattering properties for particles in different regions: in the uppermost haze layer, the scattering particles are fixed at a modified gamma size distribution with a mean of 0.1 and a variance of 0.005 μm, while all other layers contain particle size distributions with variance of 0.3 and means of {0.6, 0.8, 1.0, 1.2} μm. We test each of these four particle sizes separately, requiring all layers except the upper haze to have the same particle size distribution. We use wavelength-dependent cross-sections and asymmetry parameters derived from Mie theory for each particle size distribution. We assume methane is not depleted in the equatorial region, which was found by previous analyses (e.g. Sromovsky et al., 2012a; Irwin et al., 2012b) and later confirmed by our own analysis.

5.1.2. Results

The retrieved parameter values for each tested combination of atmospheric structure, methane profile, and particle size are shown in Fig. 6, and the corresponding values of the DIC are shown in Fig. 7. Fig. 8 plots the data alongside the model spectra corresponding to the best-fit cases of each of the three vertical structures.

We find that we are able to get an adequate fit to the data with all three atmospheric structure models: diffuse (DH), compact (2C), and combination (MDH). The different atmospheric structures find very consistent values for atmospheric characteristics that are shared between models. The fits with the DH and MDH models find similar values for the optical depths of all four aerosols layers, even though the lowest layers differ in position and compactness between the models. The MDH and 2C models both include a compact bottom cloud, and the retrieved optical depth, pressure level, and fractional scale height of this cloud are consistent between the models despite their very different structures above 2 bars. These similarities demonstrate that the retrieved vertical aerosol distribution tends toward the same profile regardless of parameterization, giving us confidence in the robustness of the solution.

We find somewhat better fits with the D1 methane profile (2.22% deep mixing ratio) than with the E1 or F1 profiles (3.20% and 4% deep mixing ratios). The D1 profile falls at the lower end of the 2–4% range found by previous authors. However, H-band observations do not provide a strong constraint on this parameter, which is additionally highly correlated with the vertical profile of scattering particles (e.g. Irwin et al., 2012b). Methane is the dominant absorber at most near-infrared and optical wavelengths, including the H-band region considered here, and the ratio of

Table 2
Atmospheric structure model parameters.

		Model 2C	Model DH	Model MDH
Upper haze	Optical depth	Free	Free	Free
	Bottom pressure (bars)	Fixed at 1.0	Fixed at 0.1	Fixed at 0.1
	Top pressure (bars)	None	None	None
	Fractional scale height	Fixed at 1.5	Fixed at 1.0	Fixed at 1.0
	Mean particle size (μm)	Fixed at 0.1	Fixed at 0.1	Fixed at 0.1
Upper middle haze	Optical depth	–	Free	Free
	Bottom pressure (bars)	–	Fixed at 1.2	Fixed at 1.2
	Top pressure (bars)	–	Fixed at 0.1	Fixed at 0.1
	Fractional scale height	–	Fixed at 1.0	Fixed at 1.0
	Mean particle size (μm)	–	Fixed at 0.6, 0.8, 1.0 or 1.2	Fixed at 0.6, 0.8, 1.0 or 1.2
Lower middle haze	Optical depth	–	Free	Free
	Bottom pressure (bars)	–	Fixed at 2.0	Fixed at 2.0
	Top pressure (bars)	–	Fixed at 1.2	Fixed at 1.2
	Fractional scale height	–	Fixed at 1.0	Fixed at 1.0
	Mean particle size (μm)	–	Fixed at 0.6, 0.8, 1.0 or 1.2	Fixed at 0.6, 0.8, 1.0 or 1.2
Lower cloud	Optical depth	Free	Free	Free
	Bottom pressure (bars)	Free	None	Free
	Top pressure (bars)	Fixed at 1.0	Fixed at 2.0	Fixed at $0.9^{*}P_{bottom}$
	Fractional scale height	Free	Fixed at 1.0	Fixed at 1.0
	Mean particle size (μm)	Fixed at 0.6, 0.8, 1.0 or 1.2	Fixed at 0.6, 0.8, 1.0 or 1.2	Fixed at 0.6, 0.8, 1.0 or 1.2

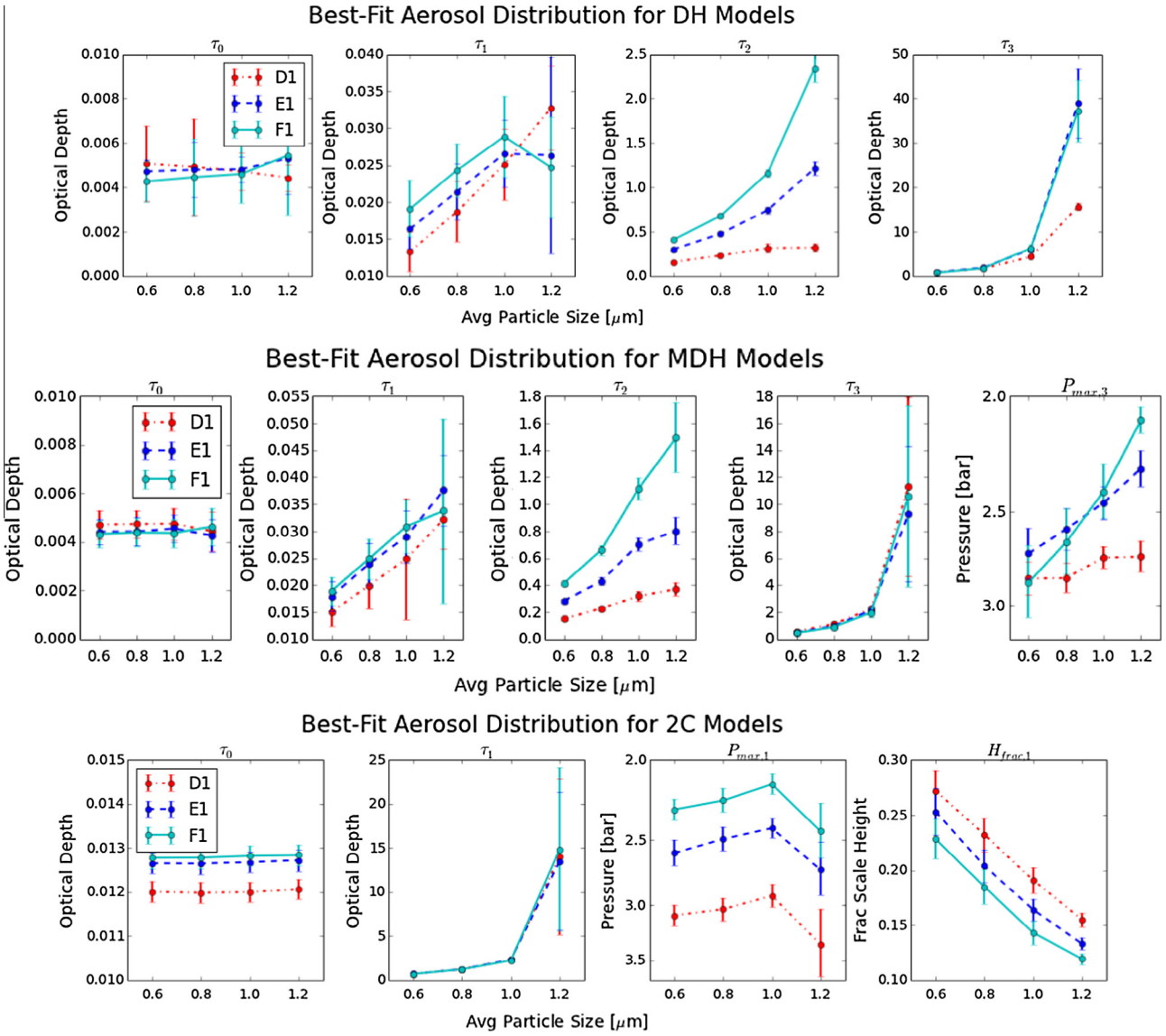

Fig. 6. Effects of model choices on best-fit parameter values: plotted are the best-fit parameter values and uncertainties for three model atmospheric structures fitted to equatorial spectra. In each plot, the *x*-axis is the mean tropospheric particle size, and the three colored curves are for the three methane profiles. Optical depths are quoted at 1.6 μm. Fig. 7 shows the quality of fit to the data for each of the models shown. (For interpretation of the references to color in this figure legend, the reader is referred to the web version of this article.)

methane to hydrogen is consequently not well measured. The narrow spectral range near 825 nm, where H_2–H_2 Collision Induced Absorption (CIA) is particularly important, provides unique constraints on the deep methane mixing ratio. Karkoschka and Tomasko (2009) used 2002 STIS observations in this spectral window to derive an equatorial deep volume mixing ratio of methane near 3%. Sromovsky et al. (2011, 2014) re-analyzed this dataset and a subsequent dataset from 2012 to infer a deep volume mixing ratio of methane near 4%. Tice et al. (2013) later used SpeX observations covering this window to derive a much lower mixing ratio, though the observations were very noisy in the relevant regime. All of these values are within the range found by Lindal et al. (1987) to be consistent with Voyager data, and Rages et al. (1991) found that the F profile in particular was needed to match Voyager observations at 0.619 μm.

We are also able to fit our data with the higher-methane F1 profile, though use of a different methane profile changes the retrieved optical depths of the various scattering layers (see Fig. 6). In particular, the choice of methane profile has a significant effect on the retrieved location of the lower cloud; fits with the F1 profile find this cloud near 2.3 bars, while fits with the D1 profile locate it closer to 3 bars. These depths are both consistent with previous two-cloud models of the uranian atmosphere using the recent sets of methane coefficients, which have consistently found the equatorial altitude of the bottom cloud in the 2–3 bar range (Karkoschka and Tomasko, 2009; Irwin et al., 2012b; Tice et al., 2013). In Section 5.2.2 we discuss the effect of methane profile choice on qualitative trends with latitude.

We are able to fit the observations with all particle sizes in the 0.6–1.2 μm range. However, we note that the choice of particle size does have a strong effect on the retrieved parameter values, even when the fit quality is comparable. This effect can be seen in Fig. 6 and is particularly pronounced in the optical depth of the 1.2–2 bar region, where larger particles correspond to higher retrieved optical depths due to their more forward-scattering phase functions.

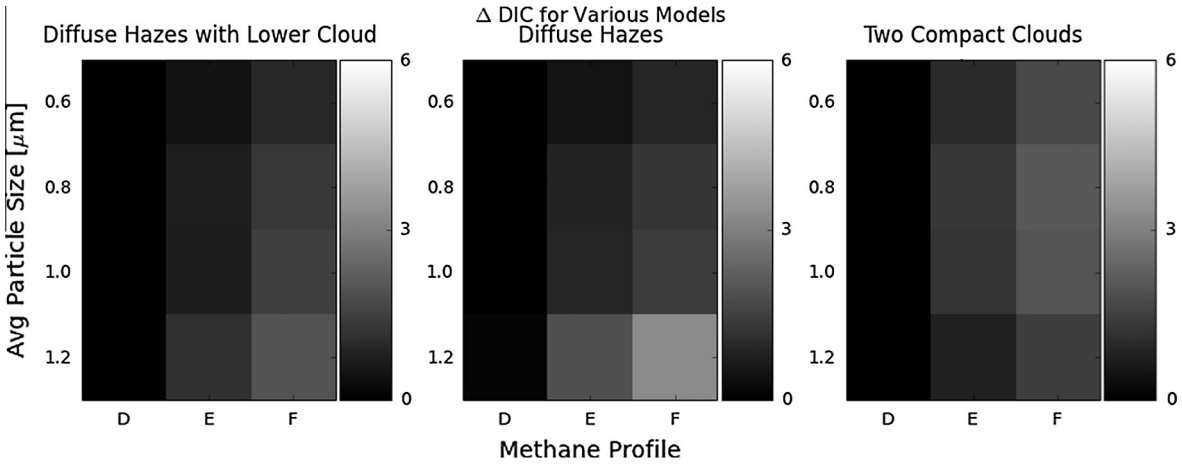

Fig. 7. Value of the Deviance Information Criterion (DIC) for model comparison, for three atmospheric structures; methane profiles D1, E1, and F1; and particle sizes of 0.6, 0.8, 1.0, and 1.2 μm. Lower values correspond to better models, and the criterion is plotted as a differential above the value for the best-fit model out of all vertical structures, particle sizes, and methane profiles. A differential of 0–2 is not significant, while a value greater than 10 nearly excludes that model; none of the parameter combinations shown are excluded by this criterion.

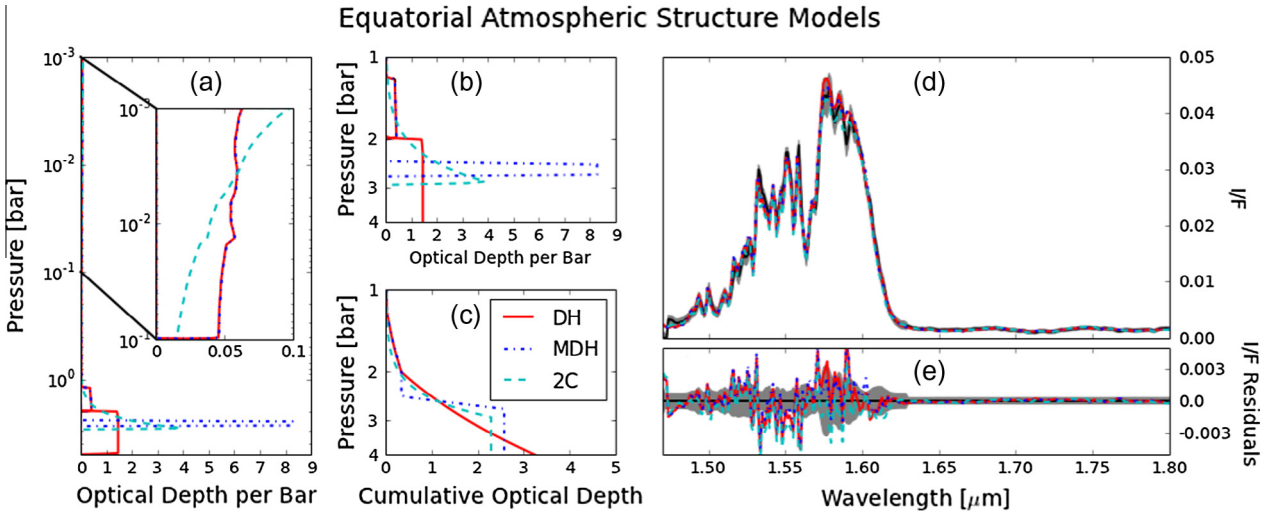

Fig. 8. A demonstration of each of three atmospheric structure models fit to equatorial data between 10°S and 10°N. The models are for diffuse hazes only (DH), diffuse hazes with a compact bottom cloud (MDH) and a two-cloud model (2C); all models shown use a methane profile with a deep volume mixing ratio of 2.22% (profile D1), and a mean particle size of 1.0 μm. The full profiles are shown in (a), with a zoom-in of the 1–4 bar region shown in both 1.6-μm optical depth per bar (b) and cumulative optical depth at 1.6 μm (c). The corresponding model spectra and residuals are shown in (d) and (e), where data are shown in black and the uncertainties are represented by the shaded region.

5.2. Latitudinal trends

5.2.1. Analysis

A knowledge of latitudinal trends in atmospheric characteristics provides important constraints on circulation models. Irwin et al. (2007) obtained the first latitudinally-resolved near-IR (1–2.5 μm) spectra of Uranus; using a model with a continuous distribution of hazes, they found two main peaks in the opacity: a deeper cloud that is thickest at the equator and thins toward the poles, and an upper layer extends from mid-southern to mid-northern latitudes and also clears toward the poles. Sromovsky and Fry (2007) imaged Uranus in seven near-IR bands with adaptive optics; they confirm that the deep cloud opacity decreases sharply toward the North pole, finding that essentially no cloud material is required to fit their observations beyond 50°N. Karkoschka and Tomasko (2009) detected latitudinal variability in 2002 HST-STIS observations at 820 nm, determining that the variations were dominated by changes in methane abundance in the 1.2–3 bar region rather than changes in aerosol opacities. Their findings, consistent with later work (e.g. Sromovsky et al., 2011), suggest that methane is increasingly depleted toward high latitudes. This result agrees with microwave observations of the deep atmosphere, which find the greatest volatile concentration in the equatorial region (de Pater et al., 1989; Hofstadter and Butler, 2003).

Recent analyses have considered latitudinal trends in both methane distribution and cloud level (Sromovsky et al., 2011, 2012a; Irwin et al., 2012a,b; Tice et al., 2013) and find that these parameters affect near-infrared observations in similar ways and are difficult to distinguish in observations at these wavelengths. Some of these studies indicate that both parameters vary with latitude, with the main cloud deck moving to higher altitudes and thinning toward the poles while the methane relative humidity decreases from equator to pole.

We use our spatially-resolved observations to investigate trends in the vertical distribution of methane and aerosols with latitude. For these fits we adopt our 2C atmospheric structure model,

the D1 methane profile with a deep volume mixing ratio of 2.22%, and a mean particle size of 1.0 μm in the troposphere. In addition, we introduce a methane depletion pressure P_d parameterizing the depth of methane depletion at a given latitude (Section 4.2.1). We perform fits with and without allowing depleted methane, and compare the effect on fit quality and on the retrieved values of the other parameters. We initially fit for the depth, opacity, and fractional scale height of both cloud layers. From these first fits, we found that the fractional scale height and location of the upper haze were poorly constrained by our models, with marginal but consistent preference across latitudes for a haze that begins at 1.0 bars or deeper with a fractional scale height between 1 and 2. We therefore fixed this layer with a base at 1.0 bars and a fractional scale height of 1.5 for our final parameter retrievals. This approach is similar to that of Tice et al. (2013), who chose to fix some of the upper haze properties for similar reasons.

We consider spectra covering latitudes from 80°S to the north polar region, in increments of 10°. However, our simulations did not converge on solutions for the most polar latitudes, and we present results only from latitudes of 70°S to 80°N.

5.2.2. Results

Retrieved trends in aerosol and methane distribution with latitude are presented in Figs. 9 and 10 and in Table 3 for two-cloud models with and without methane depletion, assuming ~1-μm particles and the D1 methane profile (2.22% deep VMR). We find that methane depletion is better able to reproduce the observations at latitudes polewards of 30° in both hemispheres than changes in the tropospheric cloud depth $P_{max,TC}$, as illustrated by the improved fit demonstrated in Fig. 9. Changing the amount of methane above the tropospheric cloud layer and changing the depth of this cloud layer both affect the methane column above the cloud, and therefore alter the model spectrum in similar ways, making it challenging to separate these two parameters (Section 5.2.1). We do find these parameters to be correlated in our retrievals, but find that while we detect no latitudinal variations in the tropospheric cloud depth beyond the level of the uncertainties, there is a clear equator-to-pole trend in the methane depletion. This result is demonstrated in Fig. 11, which plots the joint probability distribution of these two parameters for each latitude bin.

The optical depths of both cloud layers match between the models at all latitudes, but the location and vertical extent of the lower cloud diverge at latitudes beyond ~30° for models with and without depletion. Fits with an undepleted model for methane find that the lower cloud becomes higher, with the cloud altitude rising steeply from near 3 bars at the equator to <2 bars by 60°. However, when we include methane depletion as a free parameter, we find that the depth of this lower cloud layer is nearly constant in latitude. While Irwin et al. (2012b) also find more methane in equatorial over polar regions, they find that the lower cloud deck still becomes higher in the atmosphere with higher latitudes even when methane relative humidity is allowed to vary.

We find that methane becomes sharply depleted to increasing depths toward the polar regions, potentially down to tens of bars within 30° of the poles. This is consistent with the recent work of Sromovsky et al. (2014), who also measure an associated poleward lowering of their *m2* cloud layer near 1.2 bars. In the methane-depleted polar regions, the air is too dry for significant methane condensation to occur at the 1.2-bar level, except in localized upwelling regions. Because our models only extend down to 8 bars, fitted depletion depths greater than this are heavily dependent on the adopted depletion profile shape.

The broad shapes of the latitudinal trends are common between both hemispheres, but we find some significant asymmetries. Parameter values are plotted to facilitate comparison between hemispheres in Fig. 10. Both aerosol layers have a higher opacity in the northern hemisphere than at equivalent southern latitudes, and the density of both layers peaks north of the equator: between 0–10°N for the upper haze and 10–20°N for the tropospheric cloud. The most prominent asymmetry is in the methane distribution, where we find much stronger depletion poleward of 40° in the southern hemisphere than in the north. Irwin et al. (2012b) also find a greater methane enrichment in the northern hemisphere in 2010, as do Tice et al. (2013), who find the maximum methane enrichment center at 4 ± 2°S, noting that this is nearly 10° north of the enrichment found by Karkoschka and Tomasko (2009), which they suggest may be a real and seasonal change. Our data, taken one year after those used by Tice et al. (2013), find a greater enrichment of methane in the northern hemisphere with a peak enrichment just north of the equator, consistent with this trend.

The region near 45°N is characterized by a denser and higher tropospheric cloud, and a significantly less depleted methane profile, than the surrounding regions. These effects may also be present at the circumpolar zone at 45°S but on a much smaller scale. In the northern region, we find a potential reversal of these trends in the latitude band just equatorward of the bright band. We show a zoom-in of this reversal in Fig. 12, where we have subtracted out a straight line through the parameter values as a function of latitude in the 25–65°N region to accentuate these variations.

The higher opacities and methane abundance in the northern hemisphere over the south, and in the northern circumpolar band in particular, are also consistent with other post-equinox observations and may represent a seasonal trend (Irwin et al., 2012b; Tice et al., 2013). Over the 2002–2012 decade surrounding the equinox, Sromovsky et al. (2014) also noted a significant darkening at mid-southern latitudes and brightening at their northern counterparts, at wavelengths probing molecular gas absorption.

As discussed in Section 5.1.2, there is strong evidence that the equatorial region may have a methane deep volume mixing ratio close to 4%. To test the effect of this methane abundance, which is higher than that of the D1 profile used in our fits, we duplicated the latitudinal fits with the F1 profile (4% VMR). The retrieved optical depths of the TC and UH were nearly identical across all latitudes, with the main difference arising in the depth of the TC and the degree of methane depletion. The use of the higher methane abundance raised the level of the TC from around 3 bars to closer to 2.2, while increasing the depth of high latitude depletion. The trends with latitude in all parameters remained the same. We therefore consider our results for latitudinal trends robust, with some uncertainty in the aerosol layer positions and methane depletion depth due to uncertainty in the methane profile.

5.3. Discrete cloud feature

5.3.1. Analysis

Unlike Neptune, which is peppered with bright, ever-changing cloud features, Uranus is relatively devoid of discrete cloud detections. While cloud activity has been repeatedly observed at Uranus' northern mid-latitudes (e.g. Karkoschka, 1998; Sromovsky et al., 2000), the southern hemisphere beyond 45°S was thought free of cloud activity until a recent reanalysis of Voyager 2 data by Karkoschka (2015) revealed dozens of discrete features at these latitudes. Until this past year, the brightest cloud feature ever observed on Uranus was detected in 2005 with Keck II imaging and adaptive optics (Sromovsky et al., 2007); this feature, located at mid-northern latitudes, was constrained to lie in the 300–500 mb range. In August 2014, vigorous storm activity of unprecedented brightness was seen in Uranus northern hemisphere reaching up to ~330 mbar (de Pater et al., 2015). A

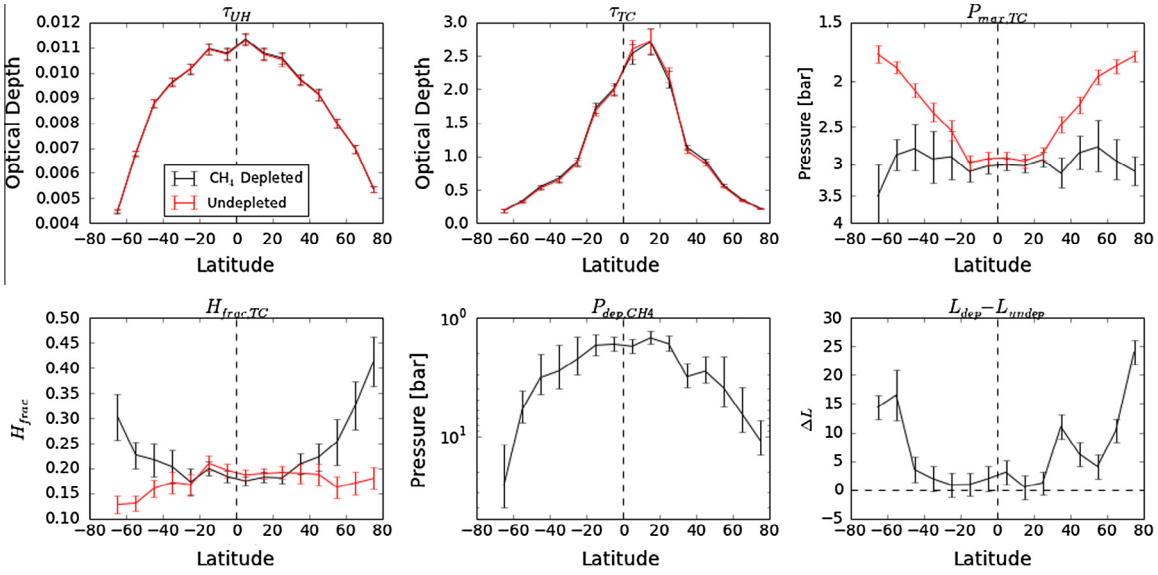

Fig. 9. Latitudinal trends in fitted parameters for a two-cloud model, including the 1.6-μm optical depth τ for the upper haze (UH) and tropospheric cloud (TC), the fractional scale height H_{frac} and altitude of the TC, and the methane depletion depth. Results are shown with and without allowing for methane depletion, and the final plot shows the improvement to the value of the likelihood function L when depletion is allowed.

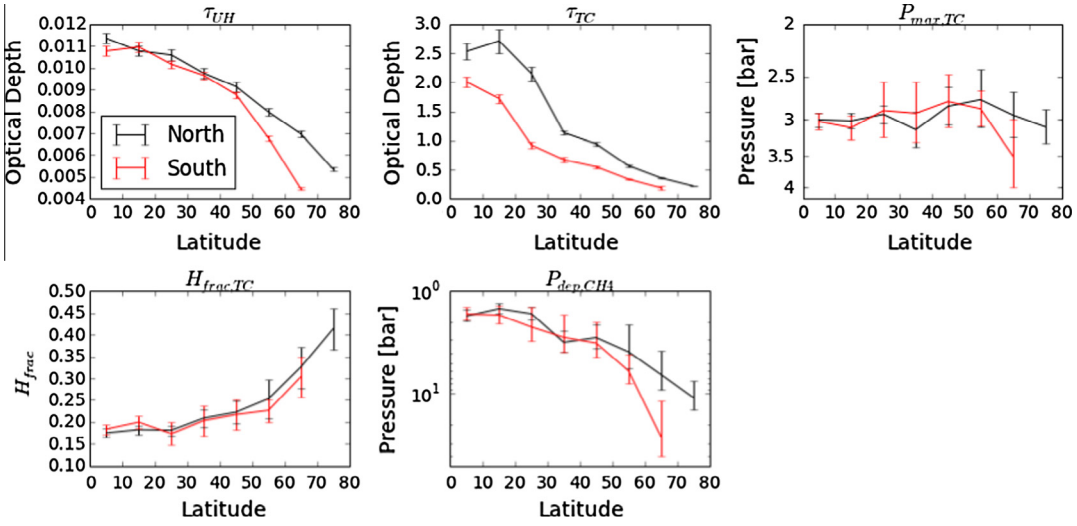

Fig. 10. Latitudinal asymmetries: variations in fitted parameters with latitude; data are the same as the depleted-methane case presented in Fig. 9, with northern and southern latitudes over-plotted to facilitate a comparison between hemispheres.

long-lived bright southern feature called the "Berg" was seen to drift from mid to equatorial latitudes, rising from near 3.5 bars to around 2 bars over three years, with pieces extending as high as ~0.6 bars (de Pater et al., 2011). Recently, Sromovsky et al. (2012b) used multi-wavelength observations to constrain the depth of a bright cloud feature and its companion near 25°N to 350–600 mb and 1.0–1.3 bar, respectively.

Sromovsky et al. (2007, 2011) argue that the position of many of the observed features so far above the 1.2-bar methane condensation level indicates that they are almost certainly composed of methane ice condensed at depth and lofted to the observed pressure levels. They postulate that this lofting could result from a deep convective event, or from local vertical displacement and condensation of atmospheric gas in the vicinity of vortex features.

In 2011 we observed a discrete cloud feature near 45°N. We extract the spectrum of this feature by calculating the reflectivity within a circular aperture centered on the feature. We find a range of aperture radii within which the choice of radius does not have a significant effect on the retrieved cloud spectrum, and choose an intermediate radius from this range for the extraction. The feature is extended, covering 50–100 pixels, and is slightly more extended in the latitudinal than the longitudinal direction.

To determine the altitude and vertical extent of this feature, we first fixed the background atmosphere at the model derived from our 2010 observations with the derived parameters for the latitude and emission angle covered by the feature. We confirm that this model provides an excellent fit to featureless regions of Uranus' disk in the same dataset.

We model the cloud feature with single- and double-component models, where we require the feature to be composed of one or two vertically-compact ($P_{top} = 0.9P_{bottom}$) layers, and fit for the pressure level and optical depth of these layers.

Table 3
Two-cloud model parameters at all latitudes.

Latitude (°)	τ_{UH}	τ_{TC}	$P_{max,TC}$ (bar)	$H_{frac,TC}$	$P_{dep,CH4}$ (bar)
−70 to −60	0.00447 ± 7e−05	0.19 ± 0.03	3.5 ± 0.5	0.30 ± 0.05	26^{+11}_{-18}
−60 to −50	0.0068 ± 0.0001	0.34 ± 0.02	2.9 ± 0.2	0.23 ± 0.03	$6.0^{+2.0}_{-2.0}$
−50 to −40	0.0088 ± 0.0002	0.55 ± 0.03	2.8 ± 0.3	0.22 ± 0.03	$3.2^{+1.0}_{-1.0}$
−40 to −30	0.0096 ± 0.0002	0.67 ± 0.04	2.9 ± 0.4	0.20 ± 0.03	$2.8^{+0.9}_{-1.0}$
−30 to −20	0.0102 ± 0.0002	0.92 ± 0.06	2.9 ± 0.3	0.17 ± 0.03	$2.2^{+0.7}_{-0.9}$
−20 to −10	0.0110 ± 0.0002	1.72 ± 0.07	3.1 ± 0.2	0.20 ± 0.01	$1.7^{+0.3}_{-0.4}$
−10 to 0	0.0108 ± 0.0002	2.00 ± 0.09	3.0 ± 0.1	0.18 ± 0.01	$1.7^{+0.2}_{-0.2}$
0 to 10	0.0113 ± 0.0002	2.5 ± 0.1	3.0 ± 0.1	0.17 ± 0.01	$1.7^{+0.2}_{-0.2}$
10 to 20	0.0108 ± 0.0002	2.7 ± 0.2	3.0 ± 0.1	0.18 ± 0.01	$1.5^{+0.2}_{-0.2}$
20 to 30	0.0106 ± 0.0002	2.1 ± 0.1	2.9 ± 0.1	0.18 ± 0.01	$1.7^{+0.2}_{-0.2}$
30 to 40	0.0097 ± 0.0002	1.14 ± 0.04	3.1 ± 0.2	0.21 ± 0.02	$3.2^{+0.7}_{-0.8}$
40 to 50	0.0091 ± 0.0002	0.94 ± 0.03	2.8 ± 0.2	0.22 ± 0.03	$2.8^{+0.6}_{-0.8}$
50 to 60	0.0080 ± 0.0002	0.57 ± 0.02	2.8 ± 0.3	0.25 ± 0.05	$3.9^{+1.0}_{-2.0}$
60 to 70	0.0070 ± 0.0002	0.359 ± 0.008	2.9 ± 0.3	0.33 ± 0.05	$6.5^{+2.0}_{-3.0}$
70 to 80	0.0054 ± 0.0001	0.220 ± 0.005	3.1 ± 0.2	0.41 ± 0.05	11^{+3}_{-4}

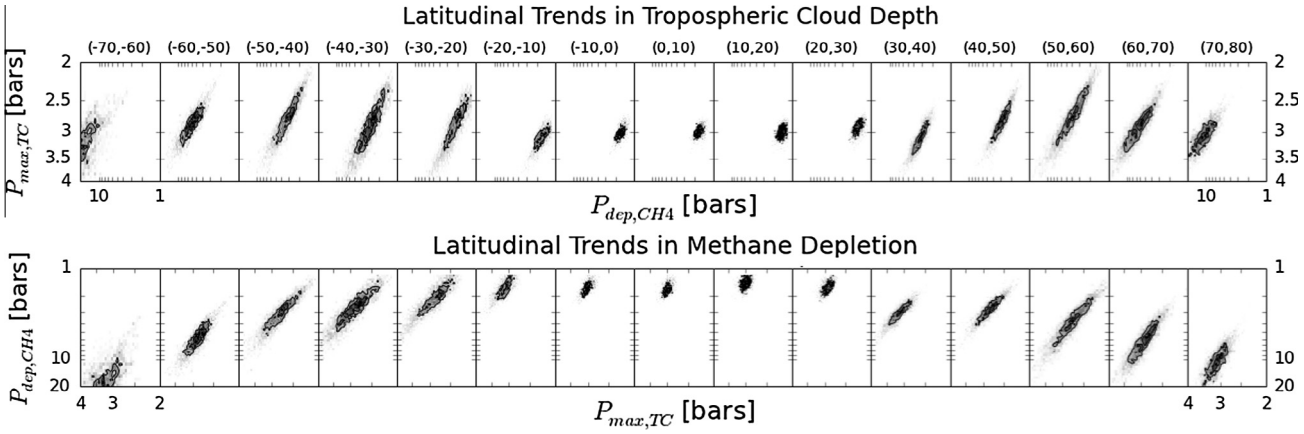

Fig. 11. 2D probability distributions for methane depletion and tropospheric cloud depth, with 30%, 60% and 90% contours. In the top row, cloud depth is plotted against methane depletion for each latitude bin; the bottom row shows the same set of distributions with *x* and *y* axes reversed. The plot for each latitude shows the correlation between the two parameters; a greater depletion depth is correlated to a greater cloud depth, and vice versa. This is because the degree of methane depletion and the depth of the tropospheric cloud affect the spectrum in similar ways through their impact on the methane column above the cloud layer. The plots of the probability distributions as a function of latitude demonstrate that we can clearly distinguish between changes in these two parameters, despite the correlation. The top panel shows that we find no significant latitudinal changes in the tropospheric cloud depth, while the bottom panel illustrates a clear trend in the methane depletion from equator to poles.

5.3.2. Results

We find that a model with two components gives an improved fit to the spectrum of the discrete cloud feature observed in 2011 over a model with only a single component, indicating a moderate vertical extent. The single-component model finds the main cloud opacity near 0.65 bars, while the double-component finds the cloud opacity focused near 0.5 and 1.3 bars. The atmospheric profiles and model spectra for each of these models are plotted in Fig. 13, and the parameters are given in Table 4.

Although our K-band OSIRIS observations of Uranus contain very low signal and we do not include them in our fits, the lack of detection of this cloud feature at these wavelengths constrains the depth of the feature. Due to the high methane absorption at these wavelengths, such observations cannot probe beneath the top ∼1 bar of the atmosphere. Though there is no detection of the feature in our OSIRIS data, the cloud is faintly discernible in K-band Keck imaging data with the NIRC2 instrument on the same night. This suggests that the bulk of the scattering particles is located below 1.0 bar with a potential small component at higher altitudes, consistent with our results from the double-component model.

Above ∼1.2 bars, methane is expected to be the most abundant condensible species in Uranus' atmosphere. Just below this level, where conditions do not permit methane condensation, the most likely condensation species may be H_2S (de Pater et al., 1991). With a base pressure at 1.2–1.4 bars, the vertical location of this cloud is therefore consistent with H_2S at the cloud base and methane in the upper region, with both species lofted upwards by a convective upwelling event. If the true base pressure is on the shallow end of our uncertainties, the cloud may be composed entirely of methane that condenses at the base of the cloud and is subsequently lofted upwards within the troposphere.

5.4. Circulation models

Circulation models for Uranus proposed in recent years include an upwelling of methane-rich gas at low latitudes, a condensation of methane in the cooler troposphere, and descent of the now methane-depleted gas back to the deep atmosphere at high latitudes (Karkoschka and Tomasko, 2009; Sromovsky et al., 2011; Irwin et al., 2012a). This picture gives a straightforward explanation for the enrichment of methane in the upper atmosphere in

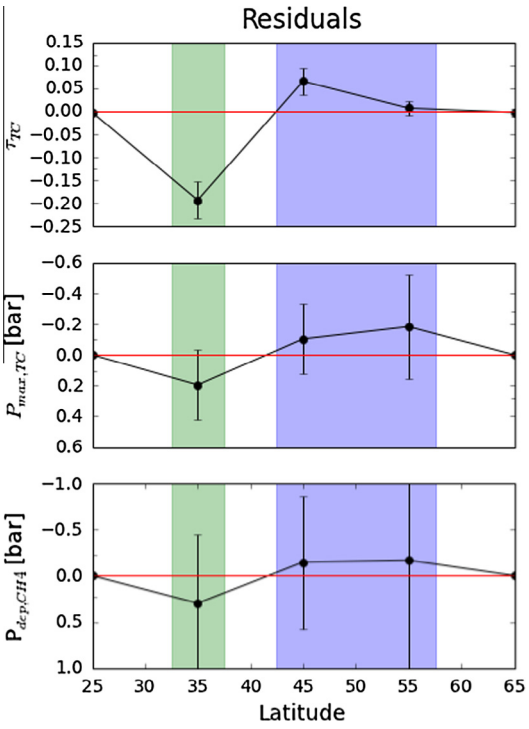

Fig. 12. Residuals in parameter values at mid-northern latitudes from a straight line through the 25–65° region, for a model that includes methane depletion. The highlighted green and blue regions indicate where we see respectively a local minimum and maximum of bottom cloud opacity and depth, and methane abundance. While only the optical depth shows a statistically-significant deviation in this region, the matching trends in the cloud depth and methane depletion depth profiles are suggestive of a real feature at these latitudes. (For interpretation of the references to color in this figure legend, the reader is referred to the web version of this article.)

the equatorial regions, but is unable to explain the existence of clouds at the depths and latitudes where they are observed.

Sromovsky et al. (2014) recently proposed a 3-layer circulation model in which the standard Hadley cell is shallow and sits on top of a counter-rotating cell at a depth of ~1.5 bars; they invoke a third cell below 10 bars with upwelling at low latitudes for consistency with microwave observations. In this model, the bright circumpolar bands are attributed to H_2S condensation clouds forming below 1.5 bars. However, such a model would inhibit equatorial condensation cloud formation below 1.5 bars, which is precisely where the global condensation cloud layer is inferred from spectral modeling.

Though the current models give explanations for some gross latitudinal trends, they do not explain hemispheric asymmetries, nor the particular location of the bright bands at 40–60°. Depletions down to 10 bars or more, as we find here and as have been previously indicated (Sromovsky et al., 2014), must be associated with deep circulation cells, but microwave observations have revealed a symmetric deep atmosphere (Hofstadter and Butler, 2003; Hofstadter et al., 2007). In addition, there is an inconsistency between the deep latitudinal variations revealed by microwave observations (de Pater et al., 1989; Hofstadter and Butler, 2003), and models of deep depletion gradients that predict wind speeds much higher than we observe (Sromovsky et al., 2011). A more complete understanding of Uranus' atmospheric circulation is clearly needed to simultaneously explain the range of observations.

If cloud features are formed in local convective upwelling events, previous authors have noted that the asymmetries in cloud occurrence between the hemispheres may be caused by the inhibition of convective cloud formation due to methane depletion (Irwin et al., 2012b; Sromovsky et al., 2014). Though the presence of depletion in both polar regions complicates this connection, evidence for a deeper depletion in the southern hemisphere offers a possible explanation for the dearth of cloud features at high southern latitudes. If the convective events producing these clouds originate at depths greater than a few bars, the southern hemisphere may be too deeply depleted to produce clouds while the northern hemisphere may contain enough methane at these depths to form them. The cloud feature we detected, which we believe originates at a depth of around 1.3 bars, is located at a local maximum of methane abundance at 45°N.

In the region just south of the bright northern band, we detect a dip in the opacity of the bottom cloud. This appears to be accompanied by an extra-deep methane depletion and a somewhat deeper cloud depth, though the deviations in these parameters are not statistically significant (see Fig. 12). This dip is present more strongly in the latitudinal trends derived by Irwin et al. (2012b) for observations during the same year, suggesting that it is a real

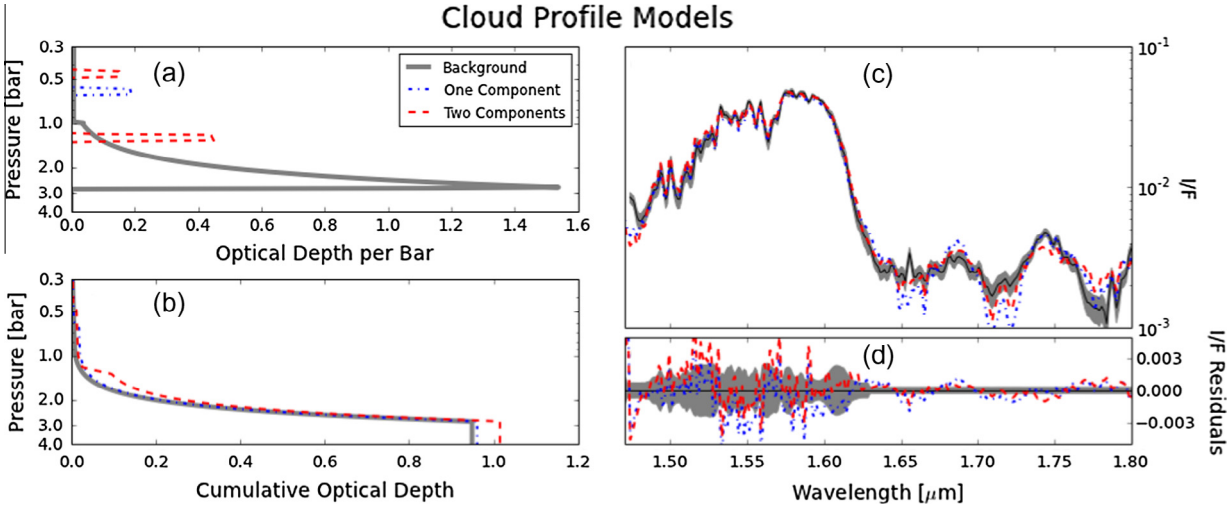

Fig. 13. Discrete cloud feature profiles and model spectra: (a) optical depth of background model and of the cloud components in the single- and double-component models; (b) cumulative optical depth for both models plotted over that of the background; and (c and d) the corresponding model spectra and residuals. Data are shown in black, and uncertainties are represented by the shaded region.

Table 4
Discrete cloud feature parameters.

Model	Optical depth	P_{max}
1-Component	0.0120 ± 0.0004	0.647 ± 0.006
2-Component	0.0074 ± 0.0004 0.059 ± 0.006	0.49 ± 0.02 1.33 ± 0.10

feature. If the circumpolar band arises from a region of local upwelling, this dip may indicate a region where the methane-depleted gas descends back into the deep atmosphere, suggesting a localized region of counter-circulation. Flaser et al. (1987) also suggested an upwelling at ±30° between 0.06 and 1 bars from Voyager IRIS measurements of lower temperatures at these latitudes, and Hofstadter and Butler (2003) noted that at the time the −45°S region was radio-dark, a potential indication of upwelling at depths of 5–50 bars.

6. Conclusions

We present the analysis of high-spectral-resolution near-infrared observations of the atmosphere of Uranus. Using radiative transfer modeling, we investigate the structure and composition of the upper atmosphere at northern and southern latitudes and at the location of a discrete cloud feature.

6.1. Aerosol structure

We find that models composed of extended scattering hazes and those containing compact clouds both provide a good fit to equatorial data. The best-fit cases of each model find a similar vertical profile of aerosol opacity whether this profile is composed of compact layers or diffuse hazes, and we therefore consider the vertical aerosol profile robust and not heavily model dependent given the vertical resolution of our observations. Our two-cloud model fits indicate that the lower cloud is moderately compact ($H_{frac} \sim 0.20$) while the density of the upper haze relative to the background gas increases with altitude ($H_{frac} > 1.0$). This is consistent with the scenario described by Pollack et al. (1987) where the constituents of the upper haze are photochemically produced in the upper stratosphere and subsequently descend, condensing near 0.1–10 mbar.

6.2. Latitudinal trends in aerosols

The optical depths of both layers in our two-cloud model decrease from equator to pole; the density of the lower cloud is sharply peaked at equatorial latitudes, while the upper haze exhibits a more gradual trend. The northern hemisphere has denser aerosols than the southern at equivalent latitudes, and the highest optical depth in each aerosol layer is reached north of the equator by up to 20°. Irwin et al. (2012b) also find a greater opacity in the northern hemisphere in both cloud layers in 2010, as well as a lower cloud layer that peaks north of the equator by ∼10°.

6.3. Methane depletion

We find methane to be undepleted in the equatorial region between 20°S and 30°N, with depletion increasing with latitude to a depth of tens of bars by ∼60° in both hemispheres, consistent with the recent results of Sromovsky et al. (2014). If we fix the methane profile across all latitudes, we find that the lower cloud shifts rapidly to higher altitudes toward the poles. However, models that include a latitudinally-varying methane abudance provide a better fit to the data and find that the altitude of the lower cloud is the same at all latitudes. We find a greater methane abundance in the northern hemisphere than the southern, again consistent with the results of Irwin et al. (2012b).

6.4. Circumpolar bands

In the bright zones near 45°S and 45°N, we find that the lower cloud is denser and higher than in the surrounding regions. These effects are more pronounced in the north than in the south, consistent with the observed fading of the southern band and brightening of the northern since the spring equinox in 2007 (Sromovsky et al., 2009; Irwin et al., 2012a). The methane abundance also reaches a local maximum around 45°N, an effect that we do not see in the southern hemisphere. In the northern hemisphere, we see weak evidence for an associated band near 30–45°N where the aerosols are thinner and deeper and methane is particularly depleted, suggestive of a region of local counter-circulation, with upwelling near 45°N and subsequent downwelling ∼10° to the south.

6.5. Cloud feature

We determine that the cloud feature observed at mid-northern latitudes in 2011 has a moderate vertical extent, with a base around 1.3 bars and extending up to the 0.5 bar level. This structure is consistent with a scenario in which a convective upwelling event lofts particles from their condensation levels to higher altitudes, indicating a composition of methane above ∼1.2 bars with a possible H_2S contribution at deeper altitudes.

6.6. Global circulation

The asymmetries between the hemispheres, including more methane, denser aerosols, and a brighter circumpolar band in the northern hemisphere, are all consistent with previously-noted seasonal trends as solar illumination falls increasingly on northern latitudes (Irwin et al., 2012a; Sromovsky et al., 2014).

The polar depletion in methane, and the accompanying decrease in aerosol optical depth, are consistent with polar downwelling down to at least a few bars. However, it is difficult to simultaneously explain the peak in aerosol opacity and methane abundance near the equator with the presence of the bright bands and cloud features at high latitudes. A better understanding of the compositions and mechanisms producing these different features would yield insight into the global dynamics at work throughout Uranus' upper atmosphere. Obtaining this information requires more observations of the uranian atmosphere at wavelengths that probe multiple altitudes and over a longer timeline; such data would place additional constraints on models, and bring us closer to a circulation model that is consistent with the full set of observations.

Acknowledgments

The authors would like to thank L. Sromovsky for helpful discussion and suggestions at various stages of this work. The near-infrared data were obtained with the W.M. Keck Observatory, which is operated by the California Institute of Technology, the University of California, and the National Aeronautics and Space Administration. The Observatory was made possible by the generous financial support of the W.M. Keck Foundation. The authors extend special thanks to those of Hawaiian ancestry on whose sacred mountain we are privileged to be guests. Without their generous hospitality, none of the observations presented would have been possible. This research was supported in part by NASA's Planetary Astronomy Program under Grant NNX07AK70G to the University of California, Berkeley. K. de Kleer is additionally

supported by the National Science Foundation Graduate Research Fellowship under Grant DGE-1106400. S. Luszcz-Cook is supported by the Kalbfleisch Postodoctoral Fellowship at the American Museum of Natural History. This research has also made use of the SIMBAD database, operated at CDS, Strasbourg, France.

References

Ádámkovics, M. et al., 2007. Widespread morning drizzle on Titan. Science 318, 962.

Borysow, J. et al., 1985. Modeling of pressure-induced far-infrared absorption spectra: Molecular hydrogen pairs. Astrophys. J. 296, 644–654.

Borysow, A., 1991. Modeling of collision-induced infrared absorption spectra of H_2–H_2 pairs in the fundamental band at temperatures from 20 to 300 K. Icarus 92, 273–279.

Borysow, A., 1992. New model of collision-induced infrared absorption spectra of H_2–He pairs int he 2–2.5 μm range at temperatures from 20 to 300 K – An update. Icarus 96, 169–175.

Borysow, A., 1993. Erratum: "Modeling of collision-induced infrared absorption spectra of H_2–H_2 pairs in the fundamental band at temperatures from 20 to 300 K". Icarus 106, 614.

Borysow, J., Frommhold, L., Birnbaum, G., 1988. Collision-induced rototranslational absorption spectra of H_2–He pairs at temperatures from 40 to 3000 K. Astrophys. J. 326, 509–515.

Campargue, A. et al., 2012. An empirical line list for methane in the 1.26–1.71 μm region for planetary investigations (T = 80–300 K). Application to Titan. Icarus 219, 110–128.

Conrath, B. et al., 1987. The helium abundance of Uranus from Voyager measurements. J. Geophys. Res. 92, 15003–15010.

de Bergh, C. et al., 2011. Applications of a new set of methane line parameters to the modeling of Titan's spectrum in the 1.58 μm window. Planet. Space Sci. 61, 85–98.

de Kleer, K. et al., 2013. Near-infrared spectra of the uranian ring system. Icarus 226, 1038–1044.

Dempster, A.P., 1974. The direct use of likelihood for significance testing. In: Proceedings of the Conference on Foundational Issues in Statistical Information on Department of Theoretical Statistics. University of Aarhus, pp. 335–352.

de Pater, I. et al., 2015. Record-breaking storm activity on Uranus in 2014. Icarus 252, 121–128.

de Pater, I., Romani, P.N., Atreya, S.K., 1989. Uranus deep atmosphere revealed. Icarus 82, 288–313.

de Pater, I., Romani, P.M., Atreya, S.K., 1991. Possible microwave absorption by H_2S gas in Uranus and Neptune's atmospheres. Icarus 91, 220–233.

de Pater, I. et al., 2011. Post-equinox observations of Uranus: Berg's evolution, vertical structure, and track towards the equator.

Fink, U., Larson, H.P., 1979. The infrared spectra of Uranus, Neptune, and Titan from 0.8 to 2.5 μm. Astrophys. J. 233, 1021–1040.

Flaser, F.M. et al., 1987. Voyager infrared observations of Uranus' atmosphere: Thermal structure and dynamics. J. Geophys. Res. 92, 15011–15018.

Foreman-Mackey, D. et al., 2013. emcee: The MCMC Hammer. arXiv:1202.3665.

Goodman, J., Weare, J., 2010. Ensemble samplers with affine invariance. Comm. App. Math. Comp. Sci. 5, 65.

Hartmann, J.M. et al., 2002. A far wing lineshape for H_2 broadened CH_4 infrared transitions. J. Qualit. Spectrosc. Radiat. Transfer 72, 117.

Hofstadter, M.D., Butler, B.J., 2003. Seasonal change in the deep atmosphere of Uranus. Icarus 165, 168–180.

Hofstadter, M.D., Butler, B.J., Gurwell, M.A., 2007. Imaging Uranus at submillimeter to centimeter wavelengths. In: AAS DPS Meeting 39, 9.07.

Irwin, P.G.J. et al., 2011. Uranus' cloud structure and seasonal variability from Gemini-North and UKIRT observations. Icarus 212, 339–350.

Irwin, P.G.J. et al., 2012a. Further seasonal changes in Uranus' cloud structure observed by Gemini-North and UKIRT. Icarus 218, 47–55.

Irwin, P.G.J. et al., 2012b. The application of new methane line absorption data to Gemini-N/NIFS and KPNO/FTS observations of Uranus' near-infrared spectrum. Icarus 220, 369–382.

Irwin, P.G.J., Teanby, N.A., Davis, G.R., 2007. Latitudinal variations in Uranus' vertical cloud structure from UKIRT UIST observations. Astrophys. J. 665, L71–L74.

Irwin, P.G.J., Teanby, N.A., Davis, G.R., 2009. Vertical cloud structure of Uranus from UKIRT/UIST observations and changes seen during Uranus' northern equinox from 2006 to 2008. Icarus 203, 287–302.

Karkoschka, E., 1998. Clouds of high contrast on Uranus. Science 280, 570–572.

Karkoschka, E., 2015. Uranus' southern circulation revealed by Voyager 2: Unique characteristics. Icarus 250, 294–307.

Karkoschka, E., Tomasko, M., 2009. The haze and methane distribution on Uranus from HST-STIS spectroscopy. Icarus 202, 287–309.

Karkoschka, E., Tomasko, M., 2010. Methane absorption coefficients for the jovian planets from laboratory, Huygens, and HST data. Icarus 205, 674–694.

Lacis, A.A., Oinas, V., 1991. A description of the correlated-k distribution method for modeling non gray gaseous absorption, thermal emission, and multiple scattering in vertically inhomogeneous atmospheres. J. Geophys. Res. 96, 9027–9064.

Larkin, J. et al., 2006. OSIRIS: A diffraction limited integral field spectrograph for Keck. In: SPIE, vol. 6269, p. 62691A.

Laver, C. et al., 2009. Component-resolved near-infrared spectra of the (22) Kalliope system. Icarus 204, 574–579.

Lii, P., Wong, M., de Pater, I., 2010. Temporal variation of the tropospheric cloud and haze in the jovian equatorial zone. Icarus 209, 591–601.

Lindal, G.F. et al., 1987. The atmosphere of Uranus – Results of radio occultation measurements. J. Geophys. Res. 92, 14987–15001.

Luszcz-Cook, S.H. et al., 2010. Seeing double at Neptune's south pole. Icarus 208, 938–944.

MacKay, D., 2003. In: Information Theory, Inference, and Learning Algorithms. Cambridge University Press.

Martonchik, J.V., Orton, G.S., Appleby, J.F., 1984. Optical properties of NH_3 ice from the far infrared to the near ultraviolet. Appl. Optics 23, 541–548.

Pollack, J.B. et al., 1987. Nature of the stratospheric haze on Uranus – Evidence for condensed hydrocarbons. J. Geophys. Res. 92, 15037–15065.

Rages, K. et al., 1991. Properties of scatterers in the troposphere and lower stratosphere of Uranus based on Voyager imaging data. Icarus 89, 359–376.

Satorre, M.A. et al., 2008. Density of CH_4, N_2 and CO_2 ices at different temperatures of deposition. Planet. Space Sci. 56, 1748–1752.

Spiegelhalter, D.J. et al., 2002. Bayesian measures of model complexity and fit. J. R. Statist. Soc. B 64, 583–689.

Sromovsky, L.A. et al., 2000. NOTE: Ground-based observations of cloud features on Uranus. Icarus 146, 307–311.

Sromovsky, L.A. et al., 2007. Dynamics, evolution, and structure of Uranus' brightest cloud feature. Icarus 192, 558–575.

Sromovsky, L.A. et al., 2009. Uranus at equinox: Cloud morphology and dynamics. Icarus 203, 265–286.

Sromovsky, L.A. et al., 2012a. Comparison of line-by-line and band models of near-IR methane absorption applied to outer planet atmospheres. Icarus 218, 1–23.

Sromovsky, L.A. et al., 2012b. Episodic bright and dark spots on Uranus. Icarus 220, 6–22.

Sromovsky, L.A. et al., 2012c. Post-equinox dynamics and polar cloud structure on Uranus. Icarus 220, 694–712.

Sromovsky, L.A. et al., 2014. Methane depletion in both polar regions of Uranus inferred from HST/STIS and Keck/NIRC2 observations. Icarus 238, 137–155.

Sromovsky, L.A., Fry, P.M., 2007. Spatially resolved cloud structure on Uranus: Implications of near-IR adaptive optics imaging. Icarus 192, 527–557.

Sromovsky, L.A., Fry, P.M., 2008. The methane abundance and structure of Uranus' cloud bands inferred from spatially resolved 2006 Keck grism spectra. Icarus 193, 252–266.

Sromovsky, L.A., Irwin, P.G.J., Fry, P.M., 2006. Near-IR methane absorption in outer planet atmospheres: Improved models of temperature dependence and implications for Uranus cloud structure. Icarus 182, 577–593.

Sromovsky, L.A., Fry, P.M., Kim, J.H., 2011. Methane on Uranus: The case for a compact CH_4 cloud layer at low latitudes and a severe CH_4 depletion at high-latitudes based on re-analysis of Voyager occultation measurements and STIS spectroscopy. Icarus 215, 292–312.

Stamnes, K. et al., 1988. Numerically stable algorithm for discrete-ordinate-method radiative transfer in multiple scattering and emitting layered media. Appl. Optics 27, 2502–2509.

Tice, D. et al., 2013. Uranus' cloud particle properties and latitudinal methane variation from IRTF SpeX observations. Icarus 223, 684–698.

Toon, O.B. et al., 1989. Rapid calculation of radiative heating rates and photodissociation rates in inhomogeneous multiple scattering atmospheres. J. Geophys. Res. 94, 16287–16301.

West, R.A., Baines, K.H., Pollack, J.B., 1991. Clouds and aerosols in the uranian atmosphere. In: Uranus. University of Arizona Press, pp. 296–324.

Williams, M.M.R., 1985. On the modified gamma distribution for representing the size spectra of coagulating aerosol particles. J. Coll. Interf. Sci. 103, 516–527.